Available online at www.sciencedirect.com

ScienceDirect

Underground Space 26 (2026) 341–363

www.keaipublishing.com/undsp

Research Paper

Preliminary risk assessment of metro lines subjected to adjacent disturbance with time-series InSAR

Zhiwen Xu [a], Suhua Zhou [a,b,c,*], Qingshan Zhang [a], Jiuchang Zhang [d], Chuting Huang [a]

[a] College of Civil Engineering, Hunan University, Changsha 410082, China
[b] Key Laboratory of Building Safety and Energy Efficiency of the Ministry of Education, Changsha 410082, China
[c] Integrated Space-Air-Ground Structural Health Monitoring and Maintenance Center, Hunan University, Changsha 410082, China
[d] Department of Information and Civil Engineering, Yunnan Minzu University, Kunming 650504, China

Received 27 March 2025; received in revised form 29 August 2025; accepted 22 September 2025
Available online 1 December 2025

Abstract

The urban metro system is a crucial infrastructure for sustainable urban development. However, ground engineering disturbances, such as foundation pit excavations and overloading, can cause damage to the metro structure, including cracks and water leakage. By integrating small baseline subset synthetic aperture radar interferometry (SBAS-InSAR) technology, this study develops a preliminary risk assessment methodology for metro lines that are subjected to ground engineering disturbances. A relevant case from Changsha was proposed, spanning from January 2017 to July 2023, using a dataset of 147 Sentinel satellite images. Key findings include: (1) InSAR technology effectively monitors ground settlement, the areas with significant construction activities, the average annual settlement rate typically exceeds −6 mm/yr, with some regions reaching up to −10 mm/yr. In contrast, most areas without ground disturbance usually experience surface settlement not exceeding −2 mm/yr. (2) Satellite imagery analysis of metro areas with settlement differences greater than 20 mm revealed that most of these regions are influenced by foundation pit excavation, and some regions may be influenced by soil consolidation. (3) Overall, metro lines in Changsha have a low risk level, with certain areas classified as "high risk". In the high-risk sections, Line 2 and Line 6 account for 32.7% and 20%, respectively, and regular inspections are required. This study would be beneficial to sustainable urban transportation.

Keywords: Surface settlement; Metro area; Risk assessment; SBAS-InSAR; Settlement velocity

1 Introduction

Urban underground space development is necessary to alleviate the pressure on urban land resources. Among these, underground transportation systems, represented by metros, effectively address issues such as urban traffic congestion (Xu et al., 2023). However, large-scale metro construction and urban underground municipal projects alter the underground stratum environment. The originally continuous underground strata are now discretely divided into independent blocks (Tan et al., 2017; Zhang et al., 2024). At the same time, the development of urban underground space changes the original seepage conditions and mechanical equilibrium of the strata, increasing the seepage interfaces of groundwater, which can lead to soil erosion in underground space (Shen et al., 2014; Liu & Tan, 2023). Long-term soil erosion in the strata can result in accidents such as stratum cavities, loose soil, and surface subsidence (Chaussard et al., 2013; Esmatkhah Irani et al., 2022; Zhang et al., 2024), posing significant challenges to urban safety and sustainable development (Ao et al., 2024). Studies have pointed out that nearly 61% of major cities in China are at risk of subsidence, threatening 36% of the urban population (Hu et al., 2004; Ao et al., 2024). There-

* Corresponding author at: College of Civil Engineering, Hunan University, Changsha 410082, China.
E-mail address: zhousuhua@hnu.edu.cn (S. Zhou).
Peer review under the responsibility of Tongji University.

https://doi.org/10.1016/j.undsp.2025.09.002

fore, it is imperative to investigate potential hazardous points on the urban surface.

To address this, scholars have conducted extensive research, developing various urban infrastructure deformation measurement methods, including precise leveling (Chakeri & Ünver, 2014; Wan et al., 2017) and global positioning system (Psimoulis et al., 2007; Ma et al., 2012). Although these monitoring techniques are technologically mature and highly accurate, they are still limited by human and material resource costs. Additionally, issues such as measurement range, monitoring point density, observation frequency, and expensive maintenance of equipment hinder large-scale, automated measurements. As a result, the information collected through these technologies is spatially and temporally constrained, leading to incomplete deformation results (Yang et al., 2022). Typically, only relative deformation at discrete points is obtained, which is insufficient for meeting the monitoring demands of large-scale infrastructure over tens of kilometers in terms of overall temporal and spatial deformation.

In recent years, some scholars have adopted synthetic aperture radar interferometry (InSAR) technology for deformation monitoring of infrastructure (Ferretti et al., 2001; Hrysiewicz et al., 2024). Early InSAR techniques primarily used SAR to acquire two or more single-look complex images of the same area from parallel orbits, forming interferograms to obtain three-dimensional surface information of the target region. Differential InSAR (DInSAR), an extension of InSAR, combines two SAR images with external terrain data to precisely measure minute surface deformations. A technique known as multi-temporal InSAR (MTInSAR) is formed by performing differential interferometry on multiple temporal images. This technique extracts deformation information from extremely stable persistent scatterer (PS) points, resulting in the development of PS-InSAR technology (Yang et al., 2018; Mehrabi et al., 2023). Some researchers have identified that PS-InSAR is prone to decoherence issues under large temporal and spatial baselines, leading to the development of the small baseline subset (SBAS)-InSAR data processing method (Cigna & Tapete, 2021). Due to its insensitivity to weather conditions and large observation range, InSAR technology has been widely applied in infrastructure monitoring (Giardina et al., 2019; Ma et al., 2022), such as monitoring slopes (Lu et al., 2023; Zeng et al., 2024), building structures (Liu et al., 2023), bridges (Qin et al., 2018), and metros (Perissin et al., 2012; Strozzi et al., 2017; Giardina et al., 2019; Yang et al., 2022), among others.

Although significant progress has been made in long-term infrastructure monitoring using InSAR technology, its application in urban metro areas still faces several challenges: (1) InSAR technology obtains deformation information of PS points by long-term surface observation. However, the surface conditions in dense urban areas are complex, and possible signal interference from various sources makes it difficult to identify the cause of ground settlement. Therefore, how to identify potential safety hazard points in the vicinity of metro areas based on surface deformation remains an urgent issue to address. (2) There is less attention paid to the potential effects of other projects in the vicinity of the metro, such as the demolition of old residential areas or the construction of new pits, on surface subsidence around the metro. These factors may pose certain safety risks and thus require adequate attention.

To address the above challenges, this study proposes a disturbance source identification method for metro areas based on SBAS-InSAR technology and satellite imagery data, aimed at assessing metro operation risks. First, Sentinel-1 satellite imagery data from January 2017 to July 2023, totaling 147 scenes, were acquired. The SBAS-InSAR processing method was applied to compute the average annual settlement rate and cumulative settlement values for the core area of Changsha. Next, a settlement difference searching algorithm was developed to calculate the settlement differences within the metro area, using satellite imagery to identify disturbance sources. Finally, metro operation risk evaluation was carried out based on the average annual settlement velocity, settlement differences, and the geology conditions of the metro bury layers. The proposed method provides an effective decision-making basis for safety monitoring in urban metro areas, particularly in identifying localized abnormal areas with significant practical value.

2 Engineering disturbances

As a representative example of urban underground space development, metro systems play a significant role in alleviating surface traffic pressure and enhancing the comprehensive utilization efficiency of urban land. However, since metro construction is typically located in city center areas, the process of construction and operation involves various potential risks and challenges. For instance, during the construction phase, the construction and operation process of tunnel excavation inevitably disturbs surrounding buildings, which, in severe cases, may lead to ground settlement and structural deformation. During the operation phase, differences in geological conditions along the tunnel alignment may result in uneven ground settlement, causing shield tunnel segments to misalign, crack, or even leak. Furthermore, as cities continue to develop, engineering activities near metro tunnels, such as adjacent excavation of foundation pits or surface loading, become unavoidable. These factors underscore the importance of conducting focused risk assessments and analyses near metro tunnels.

Figure 1(a) illustrates the foundation pit excavation above the tunnel, which involves two critical events. First, during the excavation phase, the tunnel structure undergoes unloading. Subsequently, as the superstructure is constructed, additional loads are imposed on the tunnel, creating an unloading-loading cycle. This cyclical process may induce structural cracks in the tunnel,

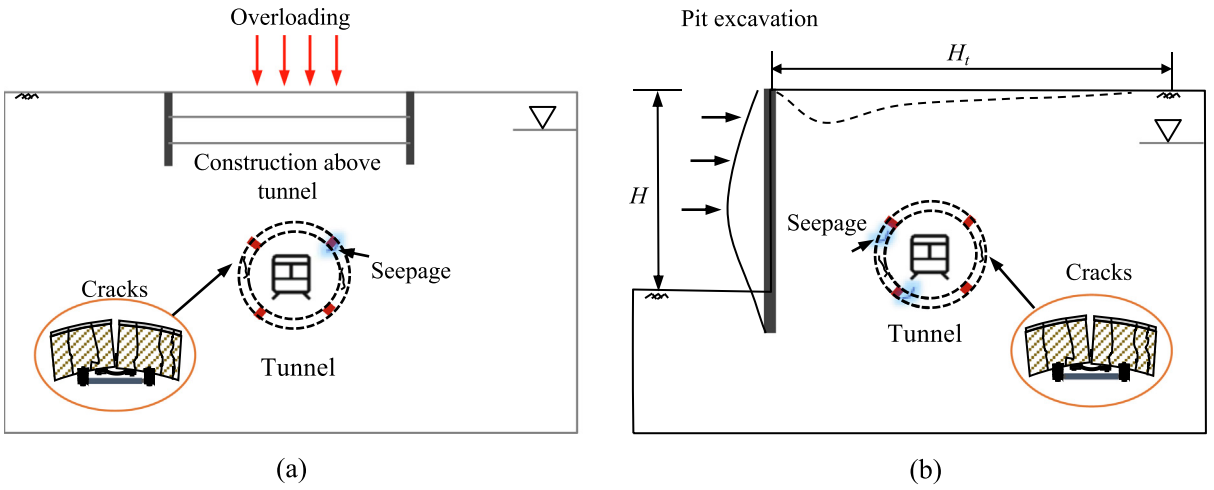

Fig. 1. Challenge cases of the metro during working hours.

potentially leading to seepage and other tunnel-related damages. Figure 1(b) shows the depth of pit excavation and the extent of impact. Determining the influence range of foundation pit excavation on the ground and adjacent buildings is crucial. According to existing standards, the recommended value for the impact range of foundation pit excavation is approximately 2–3 times the excavation depth. Based on the degree of impact, the area outside the foundation pit is divided into three zones: the primary impact zone, where $H_t < 0.7H$; the secondary impact zone, where $0.7H < H_t < (2.0–3.0)H$; and the general impact zone, where $H_t > (2.0–3.0)H$ (Ministry of Housing and Urban-Rural Development of the People's Republic of China, 2013). In addition, excavation near metro tunnels can induce both horizontal and vertical displacements. Regulatory guidelines specify that the allowable settlement for tunnel structures ranges from 3 to 10 mm, the uplift limit is 5 mm, and the permissible horizontal displacement is 3 to 5 mm. Exceeding these deformation thresholds increases the risk of structural deterioration, posing a significant threat to tunnel integrity and operational safety.

Figure 2 presents the results of a survey on metro tunnel damages in several Chinese cities. Figure 2(a) shows tunnel damage caused by adjacent foundation pit excavation along Line 2 of the Nanjing Metro. The tunnel is buried at a depth of 15 m, the foundation pit has a depth of 22.3 m, and the distance between the pit and the tunnel is 33 m. Reports indicate that the excavation of the pit caused structural cracks in the tunnel and seepage in certain areas. Figure 2(b) illustrates leakage damage in the tunnel structure of Line 10 of the Shanghai Metro due to long-term differential settlement. Figure 2(c) depicts tunnel structural damage caused by adjacent foundation pit excavation along Line 1 of the Ningbo Metro. Figure 2(d) shows concrete spalling of the structure in Line 2 of the Changsha Metro, triggered by adjacent foundation pit excavation.

Table 1 presents typical damage cases during metro operations, with disturbance sources including foundation pit excavation above or adjacent to tunnels, as well as new tunnels passing beneath existing ones. The resulting risks include structural cracking, horizontal displacement, vertical heave or settlement, leakage, and other tunnel-related damage.

Additionally, the longitudinal settlement of metro tunnels is also a critical aspect worth attention. Numerous studies have demonstrated that during the long-term operation of metro systems, geological conditions can lead to uneven longitudinal settlement of the tunnels, resulting in structural damage. This, in turn, may cause segmental leakage, further exacerbating the uneven surface settlement (Shen et al., 2014; Wu et al., 2024).

3 Methodology

During its long-term operation, metro tunnels are subject to various disturbances, which, when severe, can trigger structural damage and subsequently affect the safe operation of the metro system. Therefore, timely identification of metro damages and potential hazards is crucial for ensuring its long-term stability. However, metro tunnels are typically located beneath urban surfaces, making them highly concealed and difficult to monitor over large areas. InSAR technology offers the ability to observe long-term, large-scale ground deformations and has been widely applied in urban construction risk screening, slope risk analysis, and more. Numerous engineering cases have shown that safety risks in urban metro systems are often caused by disturbances from adjacent projects. Therefore, using InSAR technology to detect disturbance sources in the vicinity of metro tunnels, and combining this with factors such as the soil environment of the metro's service layers, holds promise for analyzing long-term settlement and potential risks of metro tunnels. The main techniques and methods used in this study are as follows.

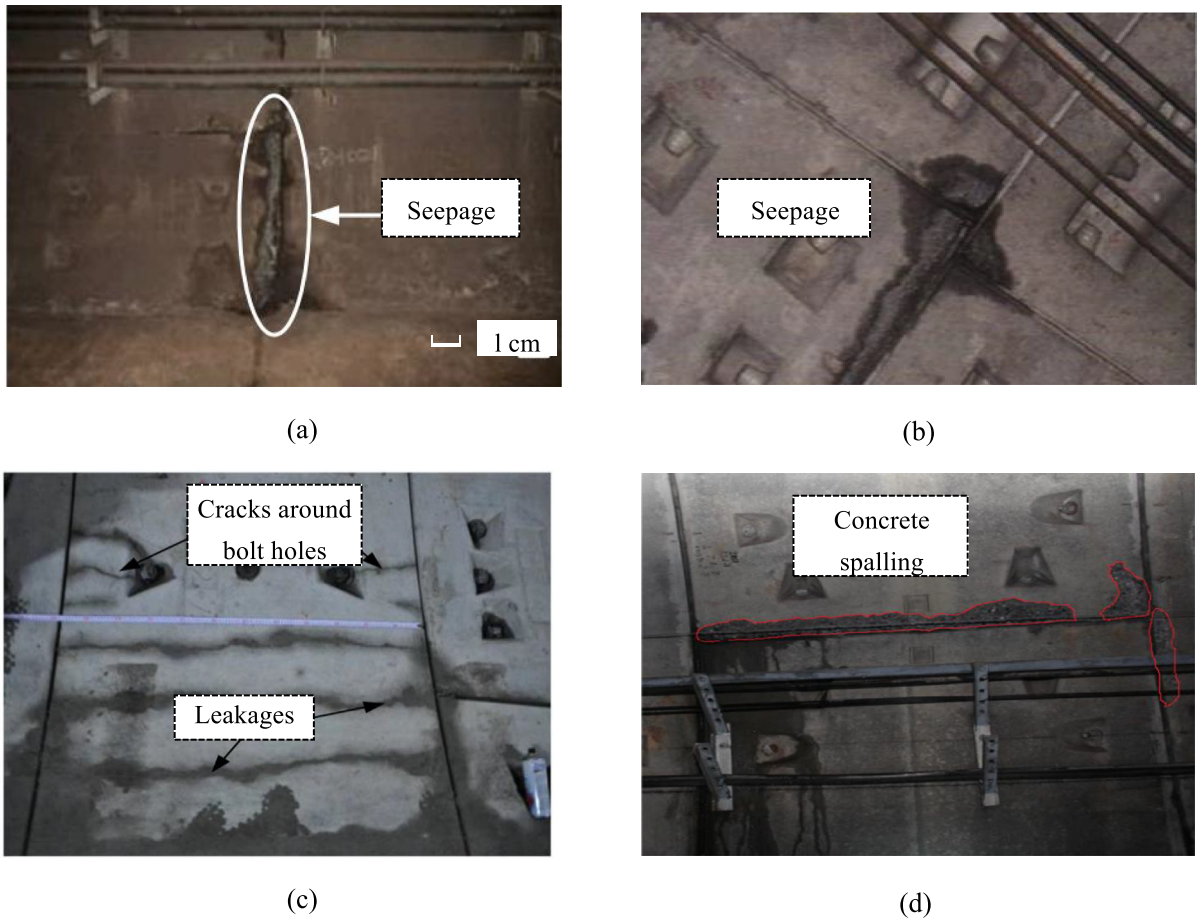

Fig. 2. Challenges of the metro during working hours. (a) Nanjing (Liu et al., 2020), (b) Shanghai (Shen et al., 2014), (c) Ningbo (Chen et al., 2016), and (d) Changsha (Huang et al., 2018).

Table 1
Damage of the tunnel under long-term operation.

Order	Disturbance	*H* (m)	*D* (m)	Damage	Reference
1	Adjacent excavation	21	14.5	Segments cracks; Concrete slab	Chang et al., 2001
2	Upper excavation	4.75	(0.3)	Tunnel bulge	Zheng et al., 2013
3	Differential settlement	–	–	Seepages	Shen et al., 2014
4	Adjacent excavation	15.0	16.5	Tunnel horizontal displacement	Zheng et al., 2016
5	Adjacent excavation	11.4	10.3	cracks and leakages	Chen et al., 2016
6	Tunelling below	–	–	Cracks	Huang et al., 2018
7	Adjacent excavation	22.3	33.0	cracks, seepages, and segment damages	Liu et al., 2020
8	Upper excavation	15.0	(3.2)	Tunnel bulge	Meng et al., 2020
9	Differential settlement	–	–	Leakage, crack	Di et al., 2021

Note: (*) is the distance from the top of the tunnel to the excavated surface of the pit; *H* is the excavation depth; *D* is the distance to the foundation pit.

3.1 Time-series InSAR technique

InSAR is an innovative space-based remote sensing technology that originated in the late 1990s and developed based on synthetic aperture radar (SAR) technology. By utilizing the phase information of SAR, InSAR successfully solves the problem of three-dimensional imaging with SAR images and can precisely acquire terrain information. At the same time, InSAR can monitor slight surface changes, enabling continuous monitoring over several years or even longer, providing high-precision and reliable surface change data on a global scale. Therefore, InSAR has unique advantages in monitoring subtle surface settlements and has become an effective technique for surface change monitoring. SBAS is a data processing technique for InSAR that originated in 2002 (Berardino et al., 2002). It combines SAR data into SBAS by setting threshold values for time and spatial baselines, thus avoiding

decorrelation in the images. This method maximizes the use of each image to improve the sampling rate of the data. SAR data within each subset have shorter time and spatial baselines, making the calculations more feasible. Within the subgroup, the least squares method is used to enhance the accuracy of data processing. Additionally, singular value decomposition (SVD) can be applied for data processing between subsets, ultimately obtaining a complete time series of settlement information. During the data processing, the SBAS method was used, and the main steps are as follows:

(1) Estimate the baseline of all SAR images, determine the spatio-temporal baseline threshold according to the short spatio-temporal baseline principle, and generate the connectivity map.
(2) All images were registered to generate the interferogram. Combined with 30-m resolution shuttle radar topography mission-digital elevation model (SRTM-DEM) data, the flat-earth and topographic phases were removed, and the differential interferogram was filtered. Specifically, the interferogram generation and filtering process is carried out as follows:

$$\Phi_{\text{interferogram}} = \Phi_1 - \Phi_2, \tag{1}$$

where Φ_1 and Φ_2 represent the phase information of the two SAR images. To remove the topographic phase (Φ_{topo}) and flat-earth phase (Φ_{flat}), SRTM-DEM data are used for phase correction, as given by the following equation:

$$\Phi_{\text{corrected}} = \Phi_{\text{interferogram}} - \Phi_{\text{topo}} - \Phi_{\text{flat}}. \tag{2}$$

Next, the differential interferogram is filtered spatially to reduce noise:

$$\Phi_{\text{filtered}} = \mathscr{F}(\Phi_{\text{corrected}}), \tag{3}$$

where $\mathscr{F}$ represents the filtering operation.

(3) High-coherence target points in the images are selected based on the coherence map. The coherence coefficient (γ) is used to evaluate the similarity of points in the images.
(4) All differential images are phase unwrapped and calibrated to convert the differential phase information into vertical deformation. The unwrapped phase information is converted into deformation using the known Rader wavelength and geometric factor K.

$$\Delta z = \frac{\Delta\Phi \cdot \lambda}{4\pi K}, \tag{4}$$

where $\Delta\Phi$ is the unwrapping phase.
(5) The first inversion is performed, a linear model is established, and the deformation rate and elevation coefficient are estimated using the matrix SVD method.
(6) A second inversion is performed to remove atmospheric effects and residual topographic phases, yielding the final average displacement rate. The PS points' three-dimensional position information is then determined, and the nonlinear deformation rate and position-time series are further calculated.
(7) After obtaining the final position-time series, necessary geographic coding and temporal analysis are performed. Spatial interpolation methods geocode the monitoring area, associating ground settlement information with actual geographic coordinates.

3.2 Differential settlement search algorithm

Surface subsidence is a common phenomenon in urban underground engineering and infrastructure construction, and accurately identifying its risks is significant for urban safety. In subsidence analysis, the presence of relative settlement differences is directly related to the stability of surface buildings and underground facilities: more considerable relative settlement differences may lead to building tilting or even collapse; in areas with significant settlement differences, secondary disasters such as surface collapse and pipeline rupture are more likely to occur (Giardina et al., 2019). The range, as an essential indicator of data dispersion, is simple to calculate and provides intuitive results, making it particularly suitable for identifying potential hazard points. Based on the range, this method constructs a surface subsidence hazard point search strategy that can be used for safety monitoring in underground spaces, metro areas, and other high-risk scenarios. The main steps and calculation process are as follows:

(1) Construction of search units. The surface raster map (such as the deformation grid generated by InSAR) is divided into several search units, each centered around a central raster point (Fig. 3(a)). The search unit's range is denoted as n, where n is the number of raster points from the center point. For example, where $n = 1$, the search unit includes a 3×3 grid of rasters (Fig. 3(b)); when $n = 2$, the search unit includes a 5×5 grid of rasters. Larger values of n can be used for large-scale analysis, while smaller values of n allow for finer localization.
(2) Raster range calculation. The range $D_{Vi,j}$ within a search unit is calculated for all raster values using the formula:

$$D_{Vi,j} = V_{\max} - V_{\min}, \tag{5}$$

where $V_{\max}$ and $V_{\min}$ are a search unit's maximum and minimum raster values, respectively. The larger the range, the greater the settlement difference in the area, indicating a higher risk.

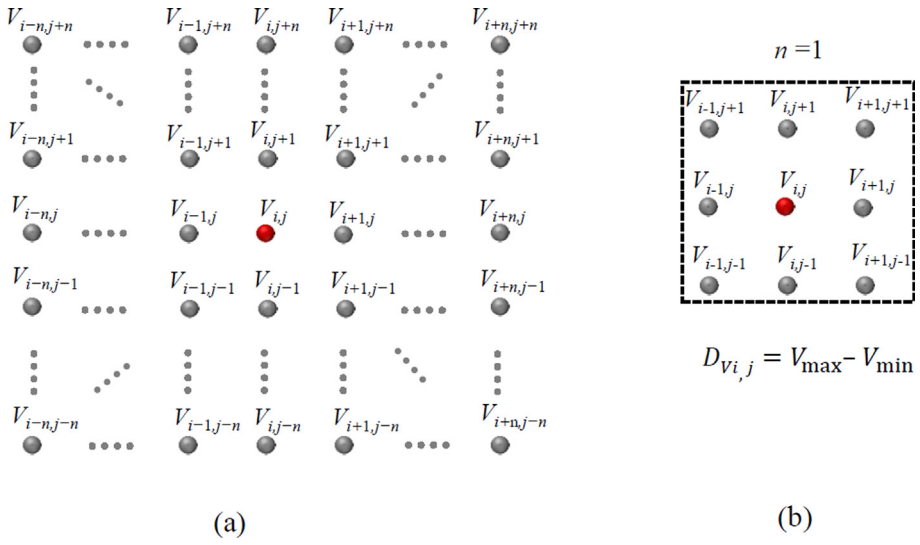

Fig. 3. Schematic diagram of hazardous point identification.

(3) Result assignment and regional classification. The calculated range $D_{Vi,j}$ of the search unit is assigned to the central raster point, and a hazard distribution map is generated to assess the regional risk level.

The pseudocode can be seen in Table 2.

Figure 4 illustrates the execution process of the search unit within the metro vicinity. Figure 4(a) provides a schematic of the metro vicinity. Figure 4(b) shows the gridded settlement values within the metro vicinity, where each number in the grid represents the settlement value for the corresponding area. The grid size typically depends on the accuracy of the InSAR data. For example, Sentinel-1 data have a positional accuracy of 10–30 m, so the grid size for settlement values is usually set between 10 and 30 m. Figure 4(c) depicts the execution process of the search unit. It shows the scenario when the search index $n = 1$, with the search unit composed of 3×3 pixels. During execution, the maximum and minimum settlement values within the search unit are first calculated. For instance, in the first step, the maximum value is 68, and the minimum value is 61; so the value for the search unit is 68 minus 61, with a final result of 7. This process continues until the settlement differences for all grids are computed.

3.3 Flowchart

This study aims to establish a metro risk analysis framework based on InSAR technology and multi-source data. As shown in Fig. 5, the study first applies small baseline InSAR technology to obtain deformation data for the study area. Then, different search units are used to calculate the settlement differences within the metro area. Next, the settlement rates in the vicinity of the metro are extracted, and risk assessment is carried out based on the metro's service-layer environment, such as the depth to bedrock and distance to the river. High-risk areas are identified, and satellite imagery is used to further analyze these regions, identifying disturbance sources and potential tunnel diseases.

Table 2
Pseudocode.

Hazard identification methods

```
# Input: grid (2D raster data), n (search unit size)
# Output: diff_map (range differences for each center point)
1. diff_map = matrix of size grid, initialized to 0 # Initialize results
for i in range (0, rows of grid):                    # Iterate over each cell
  for j in range (0, columns of grid):               # Define search unit boundaries (ensure within grid edges)
      row_min = max(0, i − n)
      row_max = min(rows of grid − 1, i + n)
      col_min = max(0, j − n)
      col_max = min(columns of grid − 1, j + n)
      # Collect all values in the search unit
      search_unit = [grid[x][y] for x in range (row_min, row_max + 1)
                     for y in range (col_min, col_max + 1)]
      diff_map[i][j] = max(search_unit) − min(search_unit) # Compute range difference and assign to diff_map
return diff_map # Return result
```

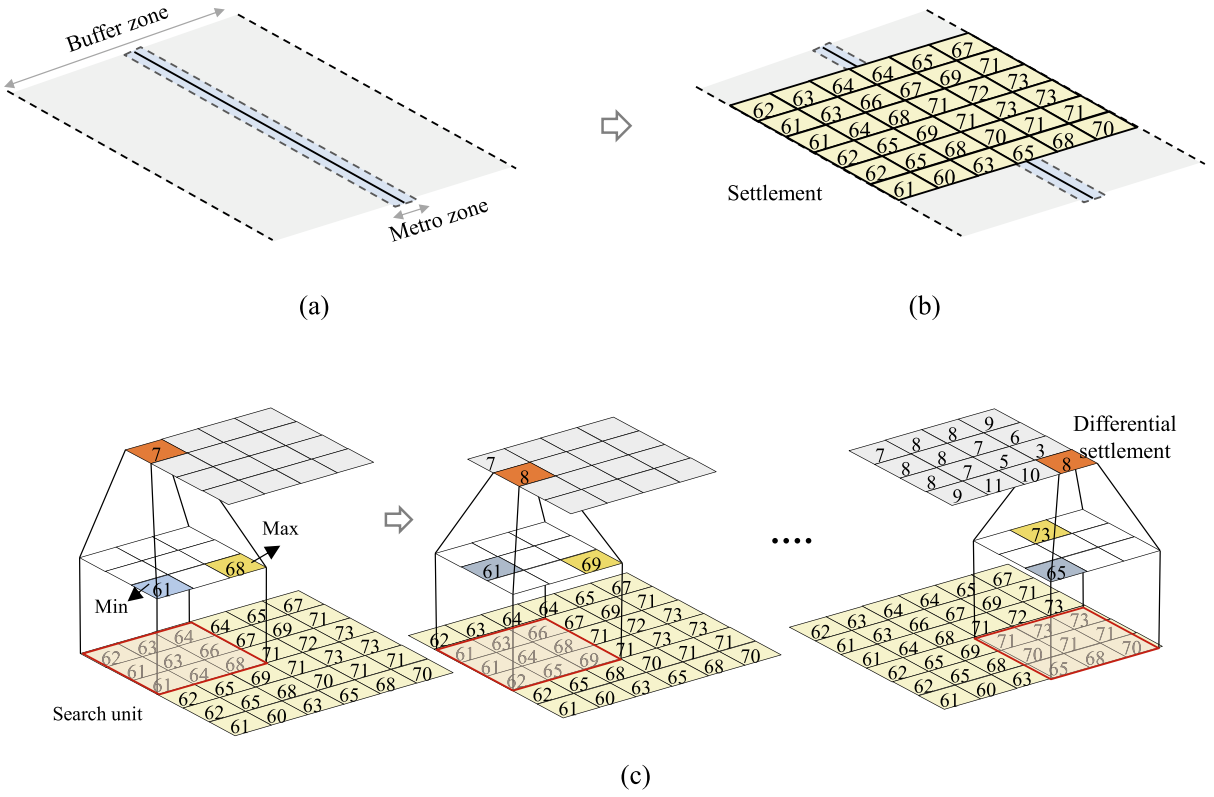

Fig. 4. Workflow diagram of the search unit.

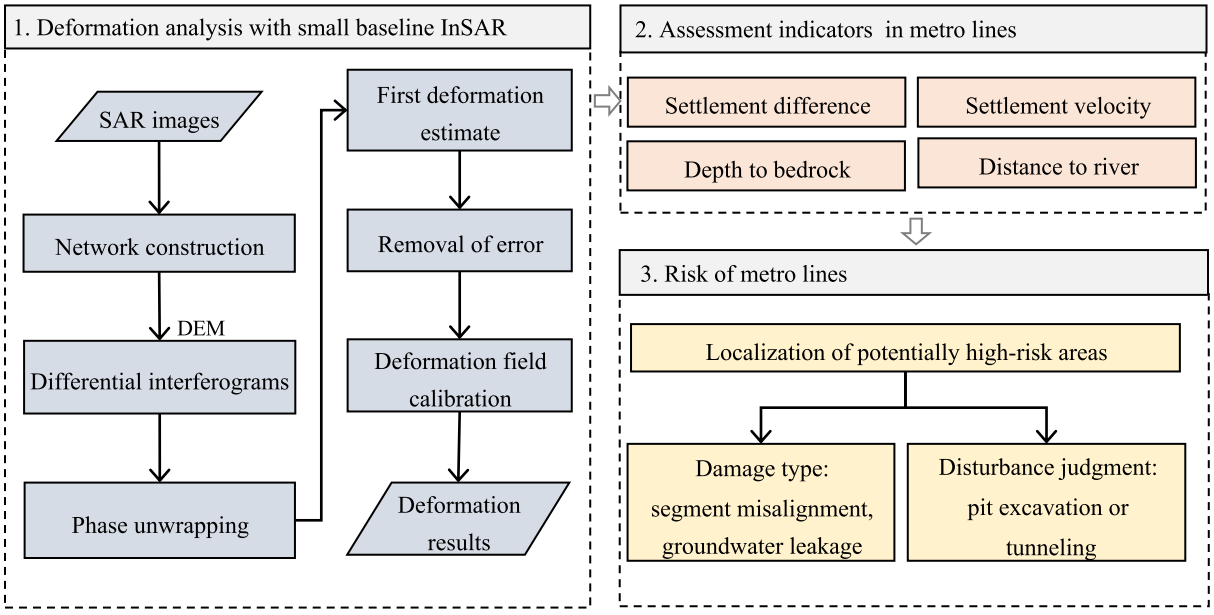

Fig. 5. Flow chart.

4 Case study

4.1 Study area

Changsha City is located in central China, in the northeastern part of Hunan Province, as shown in Fig. 6. Changsha lies between latitudes 27°51′–28°40′N and longitudes 111°53′–114°15′E. The study area is 22 km wide from east to west and 20 km long from north to south, with a core urban area covering 440 square kilometers. The city's topography is distinct, with the Xiang River dividing it into the eastern and western regions. The eastern region is relatively flat and features many tributary rivers, while the western region is more steeply inclined, with Yuelu Mountain as a representative landmark. The shallow soils in Changsha are mainly clay and silty soils, with soil layer

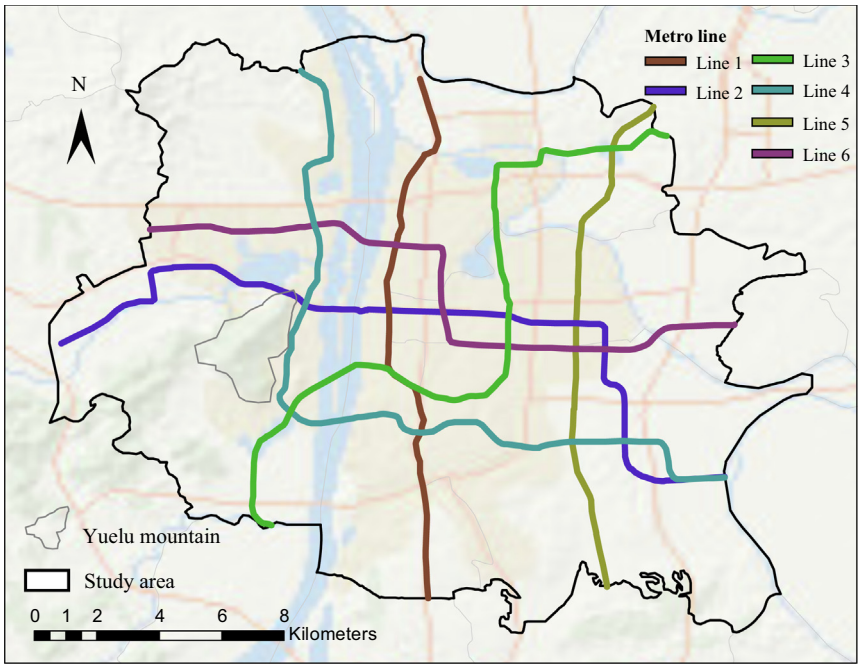

Fig. 6. Location map of the study area.

thickness ranging from 10 to 80 m, and the bedrock consists primarily of slate and granite. With the advancement of urbanization, a large influx of people has entered Changsha. Since 2010, the city has begun constructing Metro Lines 1 and 2, which were completed and opened for operation in 2016. Today, the core urban area of Changsha is served by six metro lines and one maglev high-speed line. Many new metro and excavation projects in the city have placed significant pressure on surface stability in recent years.

Changsha has been progressively constructing metro lines since 2014, with the longest-operating metro line in service for over 10 years to meet residents' transportation needs and alleviate urban congestion. Table 3 presents the construction timeline for Changsha's metro system.

4.2 Settlement velocity map

Through the SBAS-InSAR data processing workflow outlined above, the cumulative settlement in the core urban area of Changsha from January 2017 to July 2023 was obtained. The interferometric dataset consists of 147 Sentinel-1A interferometric wide swath images acquired during this period. The first step involved constructing the connection graph. Given the relatively long temporal baselines between some image pairs (e.g., the time baseline between the first and the 147th image spans nearly seven years), there is a significant risk of temporal decorrelation. To mitigate this, a temporal baseline threshold of 100 days and a spatial baseline threshold of 300 m were applied to ensure the selection of coherent image pairs. The SRTM-DEM with a spatial resolution of 30 m was used to remove the topographic phase component during interferometric processing. In addition, specific filtering parameters were optimized to reduce phase unwrapping errors. The study area is bisected by the Xiangjiang River, which ranges in width from approximately 1.0 to 1.3 km. Over water bodies, Sentinel-1A SAR data typically exhibit low coherence, making the interferometric results particularly vulnerable to noise and discontinuities. To address this, a larger filtering window (64 × 64 pixels) was employed, which helped maintain phase continuity across the river and eliminate

Table 3
Metro construction time of Changsha.

Metro line	Start of construction	Opened	Starting station	Terminal station
1	2010–12	2016–01	Kaifu District Government	Shangshuangtang
2	2009–09	2014–04	Guangda	West Meixi Lake
3	2014–01	2020–06	Shantang	Guangsheng
4	2014–12	2019–05	Guanziling	Dujiaping
5	2015–11	2020–06	Shuiduhe	Maozhutang
6	2016–12	2022–06	Xiejiaqiao	Huanghua Airport

deformation discontinuities caused by water-related decorrelation. After implementing these processing strategies, reliable and continuous ground subsidence rates across the urban area of Changsha were successfully derived.

Figure 7 shows the vertical velocity settlement in the core urban area of Changsha from January 2017 to July 2023. Positive values indicate uplift, while negative values represent settlement. As seen in the figure, the ground in the study area is generally stable. However, there are localized regions with settlement rates greater than −6 mm/yr, mainly in the eastern part of the area. The more severe settlement zones, such as Area *A* (Yuehu Street), Area *B* (Yuhuating Street), and Area *C* (Dongshan Street), are shown in the figure. Additionally, there are some small-scale regions where settlement is concentrated. Larger settlement areas are typically located near rivers, lakes, or newly developed construction zones (Xu et al., 2021; He et al., 2024).

4.3 Verification

Figure 8 shows satellite imagery and settlement velocity maps for area *A*. As seen in Fig. 8(a), the satellite imagery in 2017, the Yuehu Street can be divided into two areas, A_1 and A_2. Comparing Fig. 8(a) with (b), it is evident that A_1 has undergone significant surface changes over the past seven years, primarily due to extensive human construction. In contrast, A_2 has not experienced large-scale construction. Figure 8(c) reveals a noticeable difference in vertical surface settlement rates between A_1 and A_2 areas. Specifically, most of the areas in A_1, which have undergone substantial construction, show settlement rates greater than −6 mm/yr, with some areas exceeding −10 mm/yr. On the other hand, A_2 remains relatively stable, with most areas experiencing a settlement rate of only −2 mm/yr. Figure 8(d) illustrates the settlement rate distribution for Area *A*, where 70% of the area falls within the range of 0–5 mm/yr, 16% falls within the range of −5 to −10 mm/yr, and approximately 3% falls below −10 mm/yr.

Figure 9 presents the annual cumulative settlement cloud map for area *A*, covering the period from January 2017 to July 2023. As shown in the figure, the settlement in the region exhibits an overall increasing trend over time. The distribution of areas with significant settlement closely matches the distribution of areas with higher settlement rates, thus validating the evolution of settlement in the region.

Figure 10 presents the settlement map for area *B*. A comparison of satellite images in Fig. 10(a) and (b) reveals that the area is a man-made construction zone, including residential and road construction, which was completed by September 2022, as shown in the satellite imagery. Figure 10(c) shows the settlement rate distribution, with the majority of the settlement concentrated near P_2. Figure 10 (d) illustrates the B_1–B_2 profile results, indicating that the maximum settlement rate in the area exceeds −15 mm/yr.

Figure 11 shows the settlement conditions for area *C*. A comparison of Fig. 11(a) and (b) reveals a man-made construction zone near point P_3, with a strip-like distribution extending from north to south. Figure 11(c) presents the

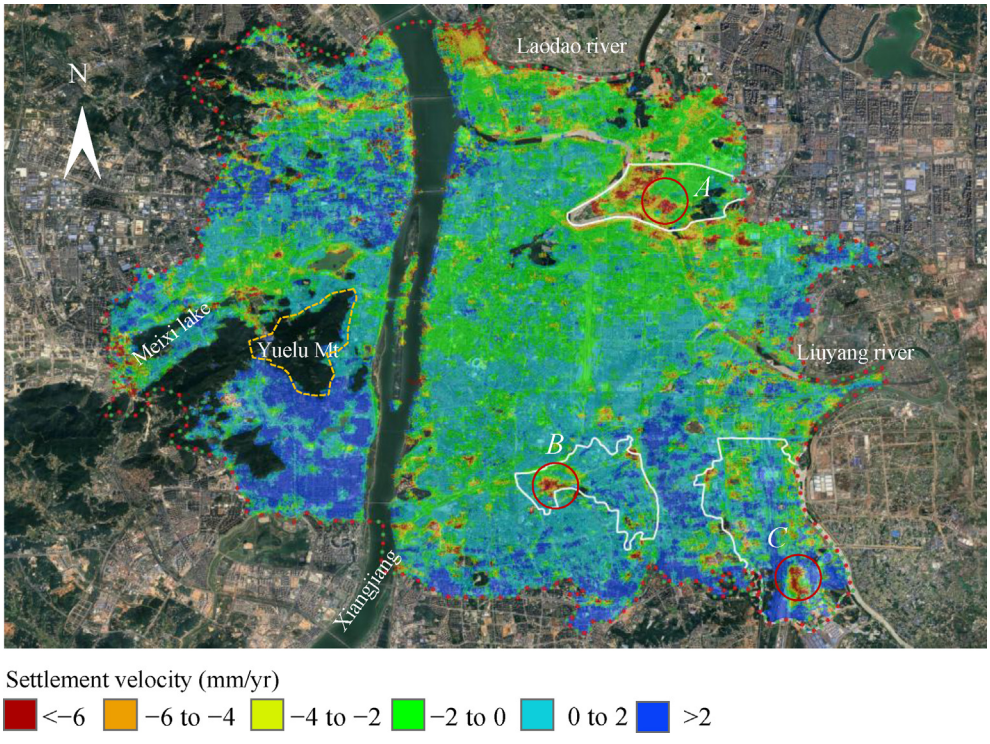

Fig. 7. Settlement velocity map of Changsha from January 2017 to July 2023.

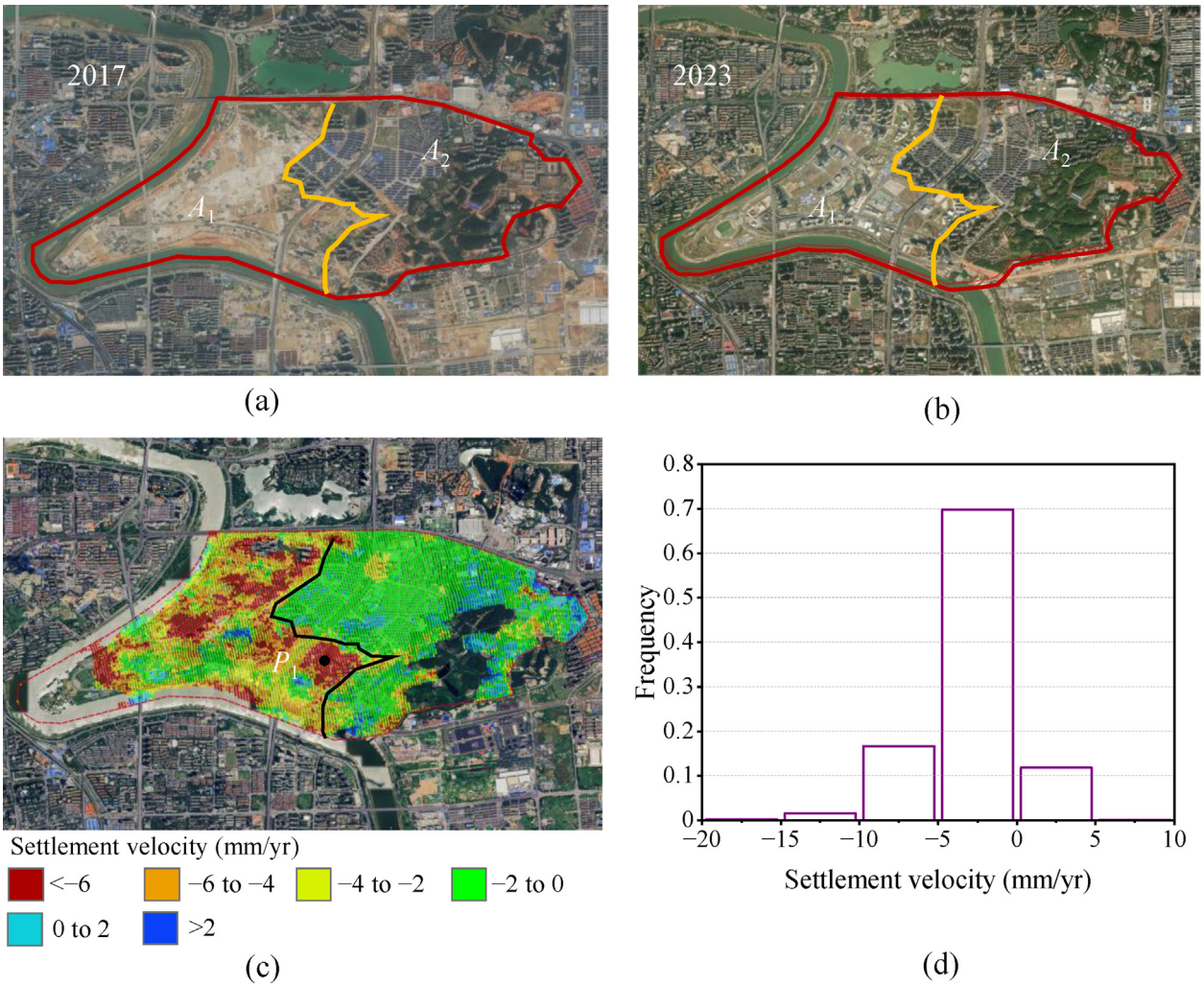

Fig. 8. Satellite imagery and settlement velocity maps for area *A*.

settlement rate map, indicating significant settlement rates in this area, with the distribution pattern matching that of the construction zone, thus validating the accuracy of InSAR in identifying construction-related disturbances. Figure 11(d) illustrates the settlement rate results along the C_1–C_2 profile, showing that the maximum settlement rate exceeds −10 mm/yr.

Figure 12 presents the time-series settlement curves of three characteristic points in areas *A*, *B*, and *C*. As shown in the figure, the maximum cumulative settlement is −100 mm. The settlement trends at the three points differ slightly. The settlement at point P_1 increases linearly overall and starts to converge towards the end of 2022. The settlement curve at P_2 can be divided into two phases: the first phase from January 2017 to June 2020, showing linear growth, and the second phase from June 2020 onwards, where the settlement reaches approximately 50 mm and then stabilizes, likely due to the cessation of construction activities after completion. The settlement curve at P_3 can also be divided into two phases: the first phase from January 2017 to June 2020, with slow settlement, and the second phase from June 2020 to July 2023, where the settlement rate initially increases, then gradually decreases, and eventually stabilizes.

The analysis demonstrates that InSAR technology effectively captures surface settlement caused by human activities. However, it is important to note that InSAR assumes a relatively stable ground surface. For activities such as the construction of new buildings or extensive leveling of mountainous areas, actual elevation changes can range from several meters to tens of meters, which may not be fully reflected in the absolute values derived from InSAR data. Nevertheless, InSAR technology can still effectively identify areas of human construction. Therefore, combining InSAR-based settlement data with satellite imagery holds promise for identifying disturbance sources within metro areas.

4.4 Risk of metro lines

As the arterial transportation system of a city, metro lines play a crucial role in urban economic development

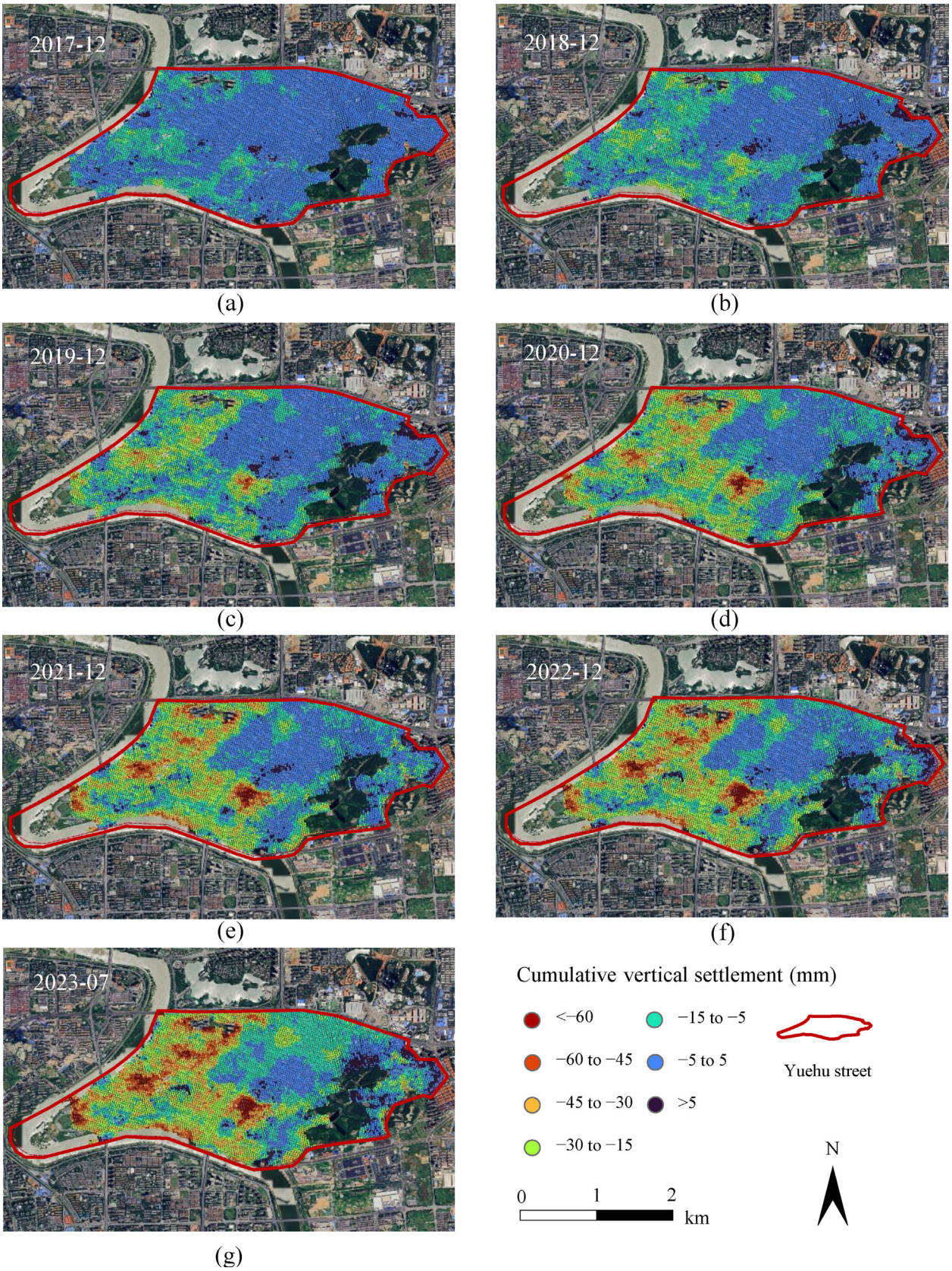

Fig. 9. Annual cumulative vertical subsidence cloud map for area *A*.

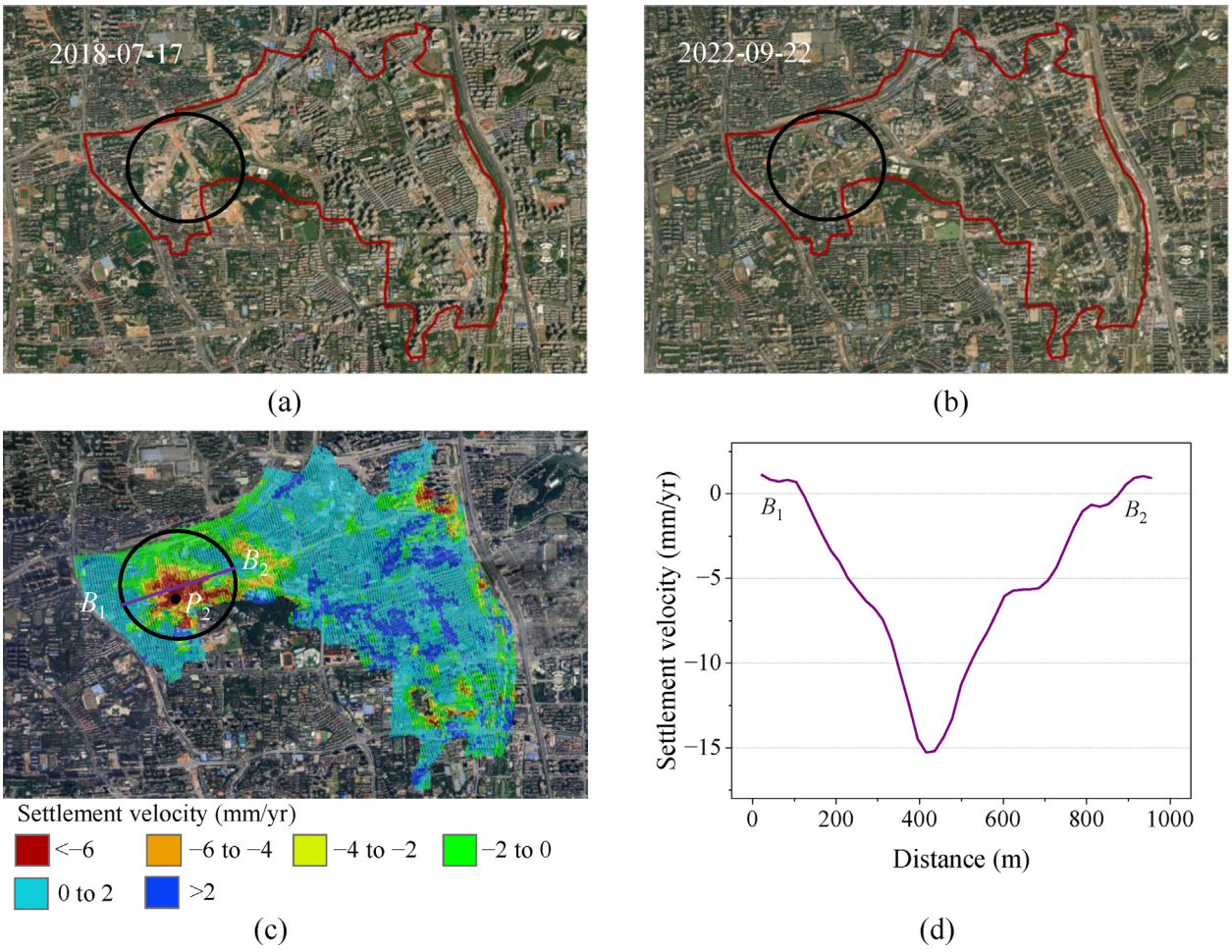

Fig. 10. Satellite imagery and settlement velocity maps for area *B*.

and residents' social life. To ensure the safe operation of urban metro systems, this section conducts a risk assessment for the operational metro lines in Changsha City using an analytic hierarchy process (AHP) method. The AHP method is a classical multi-factor decision-making method widely used in infrastructure risk assessment (Saaty, 1994; Doyle, 2016; Zhou et al., 2019).

4.4.1 Assessment indicators

In selecting evaluation indicators, two main categories were considered: the first category includes InSAR observation data, specifically the S_1 average settlement rate and S_2 settlement differences in metro lines. The second category includes the factors related to the metro's service strata, including S_3 depth to bedrock and S_4 distance to river. Previous studies have shown that metro systems are susceptible to disturbances from nearby construction activities during long-term service, where excavation-induced disturbances can be identified through the S_1 settlement rate and S_2 settlement differences. Moreover, research indicates that variations in soft soil thickness can lead to differential settlement, which may cause shield tunnel segments to misalign, crack, or experience water leakage.

Figure 13 shows the indicators used to assess the risk of the metro lines. Figure 13(a) illustrates the settlement velocity within the metro area. As depicted, the settlement velocity in most of the metro area is less than −2 mm/yr, while some regions exhibit relatively higher settlement rates. Figure 13(b) presents the settlement difference results, which represent the settlement variation within a certain range around the metro area. A larger settlement difference indicates a higher degree of disturbance in the region. The figure shows that most sections have a settlement difference of less than 15 mm, while some areas exceed 45 mm. Figure 13(c) shows the distance to the bedrock, with larger values indicating thicker loose soil layers, typically ranging from 20 to 50 m. Figure 13(d) illustrates the distance to rivers, highlighting the developed water systems in Changsha. Table 4 presents the classification of the four parameters, where the evaluation labels represent the impact degree of different values on the metro line. Larger values indicate a greater impact on the metro.

4.4.2 Assessment model and result

To assess the impact of each factor on the metro line, AHP method is used to determine the weight of each

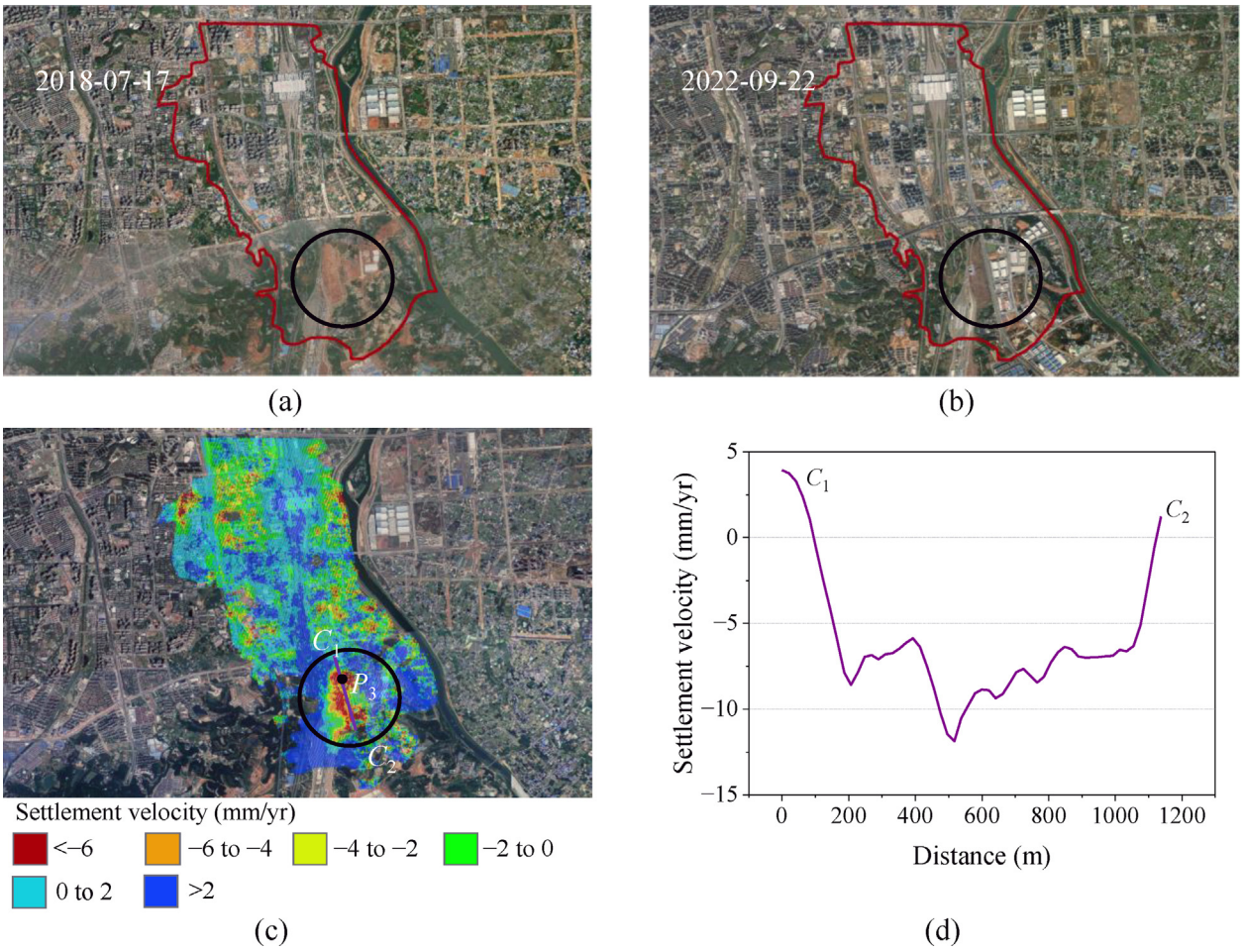

Fig. 11. Satellite imagery and settlement velocity maps for area *C*.

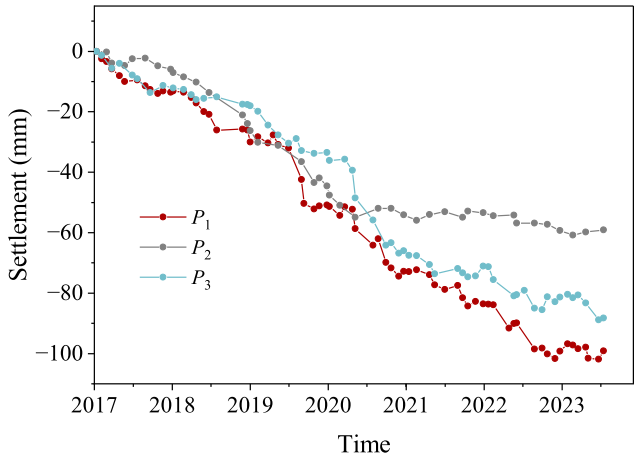

Fig. 12. Time-series settlement for different points.

parameter and ultimately calculate the risk score, which is then used to classify the risk level. Table 5 presents the importance judgment matrix, which is derived from expert evaluations. In the expert rating process, experts assess the relative importance between pairs of factors. The results obtained are as follows:

$$b_{ij} = \frac{a_{ij}}{\sum_{k=1}^{n} a_{kj}}, \tag{6}$$

$$W_i = \frac{\sum_{j=1}^{n} b_{ij}}{\sum_{i=1}^{n} (\sum_{j=1}^{n} b_{ij})}, \tag{7}$$

$$R = \sum_{k=1}^{n} S_k * W_k. \tag{8}$$

In this analysis, each evaluation factor is classified into four levels based on its potential threat to the tunnel structure. First, Table 5 is normalized using Eq. (6) to obtain the standardized results. Then, the weight of each factor is calculated using Eq. (7), followed by the computation of the risk evaluation score using Eq. (8). Finally, the risk scores are normalized and classified into four levels—very high, high, low, and very low—using a uniform classification method. Following the Technical standard for maintenance of tunnel structures in urban rail transit (Tongji University et al., 2018), a semi-quantitative approach is adopted to establish the risk level classification. The detailed classification criteria are presented in Table 6.

Figure 14 illustrates the risk assessment results for the metro system in Changsha. The risk levels are classified into four categories: very high, high, low, and very low.

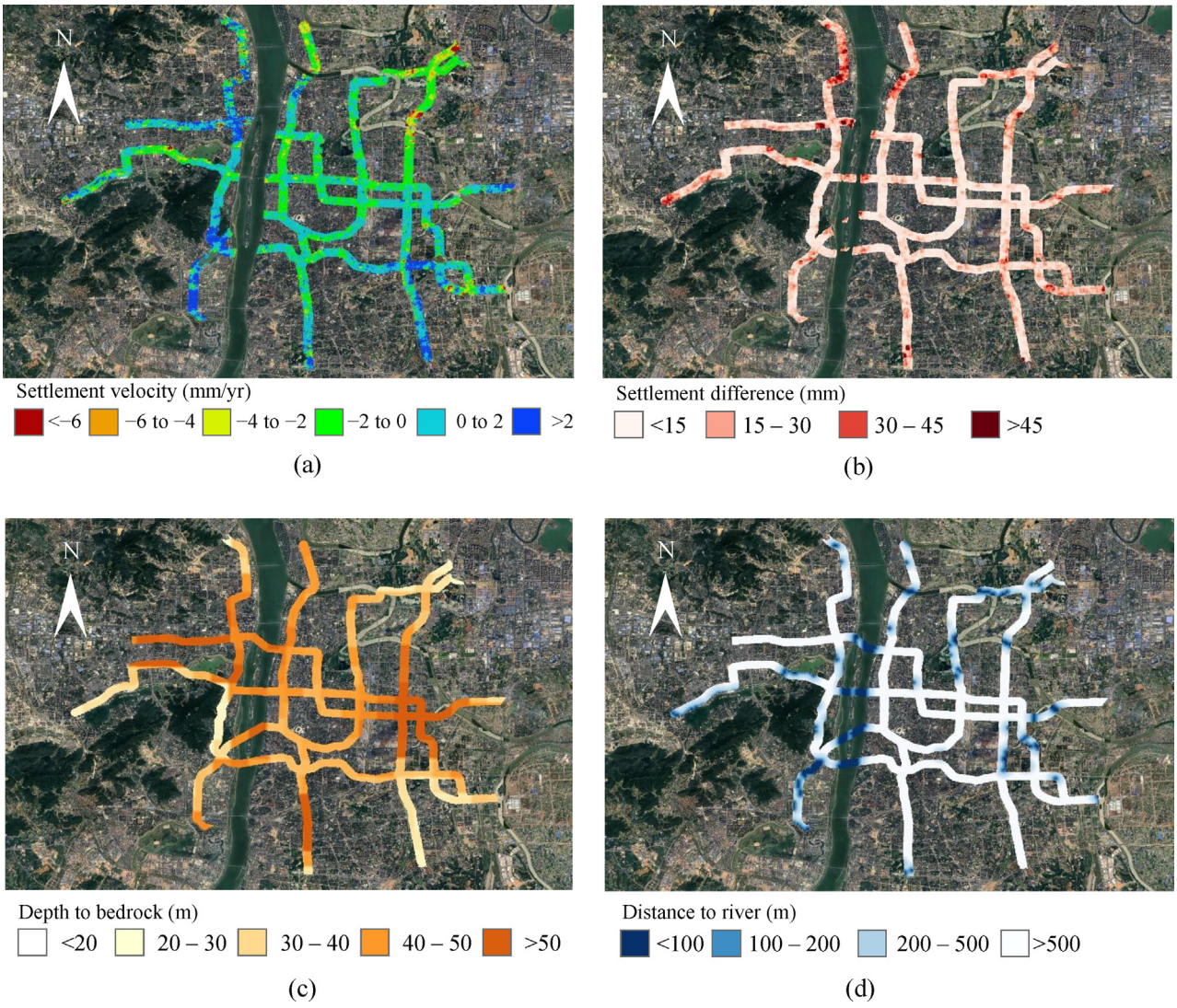

Fig. 13. Indicators used to assess the risk of the metro lines.

Table 4
Categorization and labels of the indicators.

Indicator	Unit	Evaluation label			
		1	2	3	4
S_1: Settlement velocity	mm/yr	>0	−2 to −4	−4 to −6	<-6
S_2: Settlement difference	mm	<10	10–20	20–30	>30
S_3: Depth to bedrock	m	<20	20–40	40–60	>60
S_4: Distance to river	m	>500	500–200	200–100	<100

Note: The data on depth to the bedrock were obtained from Yan et al. (2020). The data of distance to river were obtained from OpenStreetMap (https://www.openstreetmap.org).

Overall, the metro system in Changsha is primarily in the low or very low risk categories, with some areas identified as high risk and very few areas classified as very high risk. As shown in the figure, the very high-risk areas are mainly concentrated in the T_1 to T_8 sections. Some tunnel sections of Line 2 (T_6, T_7, T_8) marked with arrows indicate known metro disease zones, primarily involving issues such as water seepage, concrete spalling, and cracks (Huang et al., 2018).

Figure 15 shows the risk statistic results of Changsha. Figure 15(a) illustrates the proportion of sections under different potential hazard levels for the six metro lines in Changsha. As shown in the figure, the proportion of sections with a "very low" hazard level ranges from 76% to

Table 5
Importance judgment matrix and the weight of factors.

	S_1	S_2	S_3	S_4	Weight
S_1	$a_{11} = 1$	$a_{12} = 1$	$a_{13} = 2$	$a_{14} = 2$	0.3357
S_2	$a_{21} = 1$	$a_{22} = 1$	$a_{23} = 2$	$a_{24} = 2$	0.3357
S_3	$a_{31} = 1/2$	$a_{32} = 1/2$	$a_{33} = 1$	$a_{34} = 1/2$	0.1284
S_4	$a_{41} = 1/2$	$a_{42} = 1/2$	$a_{43} = 2$	$a_{44} = 1$	0.2003

Note: a_{ij} denotes the comparative results of the ith factor with respect to the jth factor, where 1 means equally important and 2 means i is more important than j, where $a_{ij} = 1/a_{ji}$.

89%, which is relatively stable. The proportion of sections with a "high" hazard level is below 5%, with Metro Line 2 having the smallest proportion of "high" sections. Figure 15(b) shows the proportion of each metro line with the "high" risk level. It can be observed that Metro Line 2 and Metro Line 6 account for 32.7% and 20%, respectively, while Metro Line 5 has the smallest proportion at 8.5%. Therefore, Metro Lines 2 and 6 in Changsha should be closely monitored during subsequent operations.

Table 6
Categorization of risk level.

Category	Score	Description	Maintenance measures
Very low	0–0.25	Negligible risk, no impact on structural safety	Regular maintenance
Low	0.25–0.50	Potential minor damage, currently no impact on tunnel structural safety	Routine upkeep and regular inspections
High	0.50–0.75	Potential moderate damage may affect tunnel structural safety in the future	Routine upkeep with increased inspection frequency
Very high	0.75–1	Possibly serious damage already present, affecting tunnel structural safety	Special monitoring as needed; decide on repair measures based on monitoring results

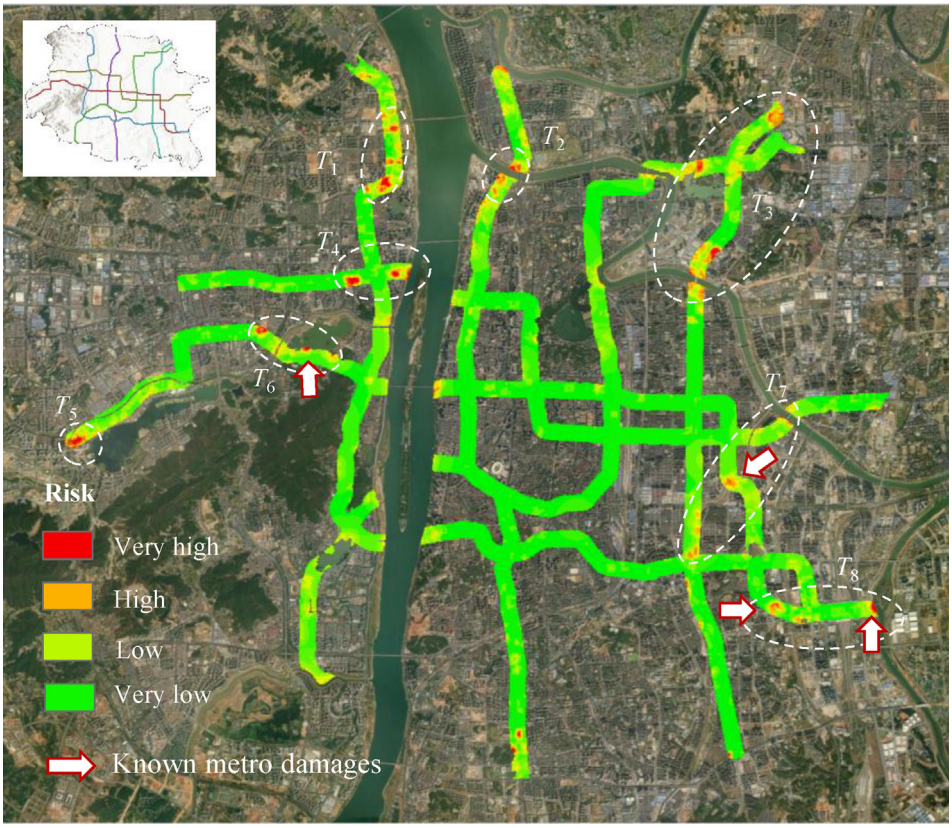

Fig. 14. Metro risk assessment results map of Changsha.

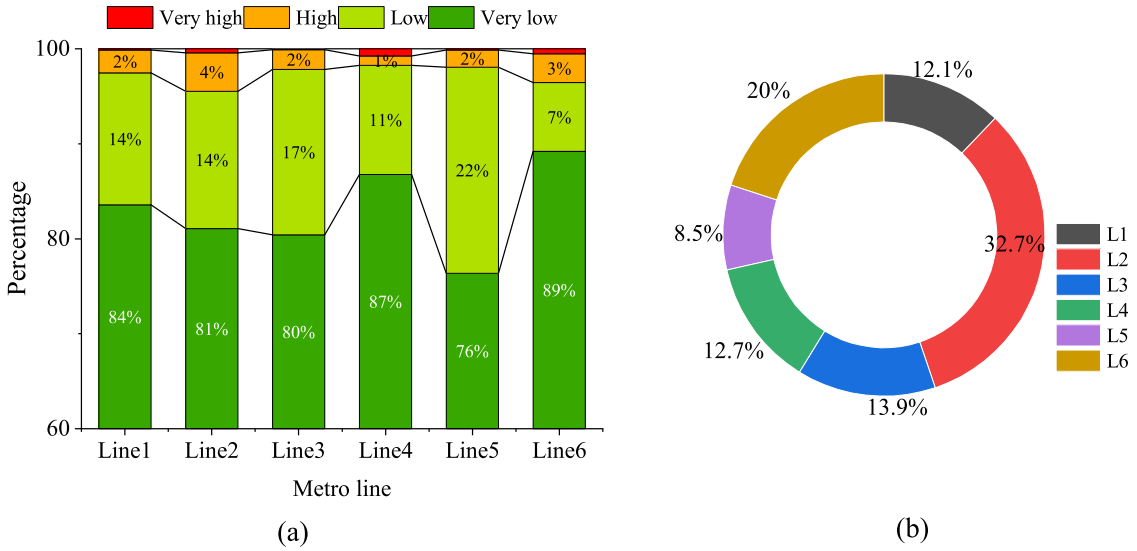

Fig. 15. Risk statistic results for Changsha Metro Line.

5 Discussions

5.1 Settlement difference search range

The above study demonstrates that InSAR technology can effectively identify surface settlement. The research indicates that human construction activities primarily cause significant ground settlement.

Figure 16 shows the two types of search units of the settlement difference of Metro Line 2. Figure 16(a) shows the results for search unit $n = 1$, with a search range of 3×3 and a grid size of approximately 20 m, resulting in a total search range of 60 m. As seen in the figure, most areas have settlement differences smaller than 5 mm, with only a few sections showing differences greater than 20 mm. Figure 16(b) presents the settlement difference search results for search unit $n = 2$, where the search range is expanded to 5×5, corresponding to a 100 m area. Compared to the first case, the regions with settlement differences greater than 20 mm have increased, particularly in six sections. According to the standards, the impact range of foundation pit excavation is 2–3 times the excavation depth, with common excavation depths ranging from 10 to 30 m. Therefore, both 60 and 100 m search ranges are suitable for analyzing disturbance risks in the metro area.

Figure 17 presents the correlation chart of settlement differences between the two search units. The x-axis represents the settlement differences along the metro line with a 3×3 search unit, while the y-axis represents the settlement differences with a 5×5 search unit. As shown in the figure, there is an overall positive correlation, and numerically, the 5×5 search unit better highlights the characteristics of differential settlement.

5.2 Disturbance identification

Based on the previous study, it is evident that the metro vicinity is prone to various disturbances. Therefore, this section analyzes the disturbance sources using settlement difference data and satellite imagery. The main approach is to first locate the areas with significant settlement differences, then use historical imagery of these areas to investigate the types of disturbance sources and their spatial relationship with the metro lines.

Figure 18 presents the cumulative settlement results of Metro Line 2 along with the settlement difference results from two search methods. The x-axis represents the mileage, the left y-axis shows the cumulative settlement values, and the right y-axis indicates the settlement difference. As seen in the figure, areas with larger cumulative settlement generally correspond to larger settlement differences. There are six segments in the figure where the settlement difference exceeds 20 mm.

Figure 19 presents the before-and-after satellite imagery comparison of six regions along Metro Line 2. The images show the regions from L2-1 to L2-6. The red markers indicate areas where significant changes in topography occurred. For example, Fig. 19(a) shows that in July 2018, the area was green space, while in September 2022, it became a high-rise building. This change indicated that excavation and construction took place during this period. The area is located south of the metro station, making it a major source of disturbance for the metro line. Similarly, Fig. 19(b) corresponds to the 2nd region with significant settlement differences, where the disturbance source is located to the north of the metro line, and the area also experienced a transition from green space to high-rise buildings. Figure 19(c) shows the L2-3 region, where the

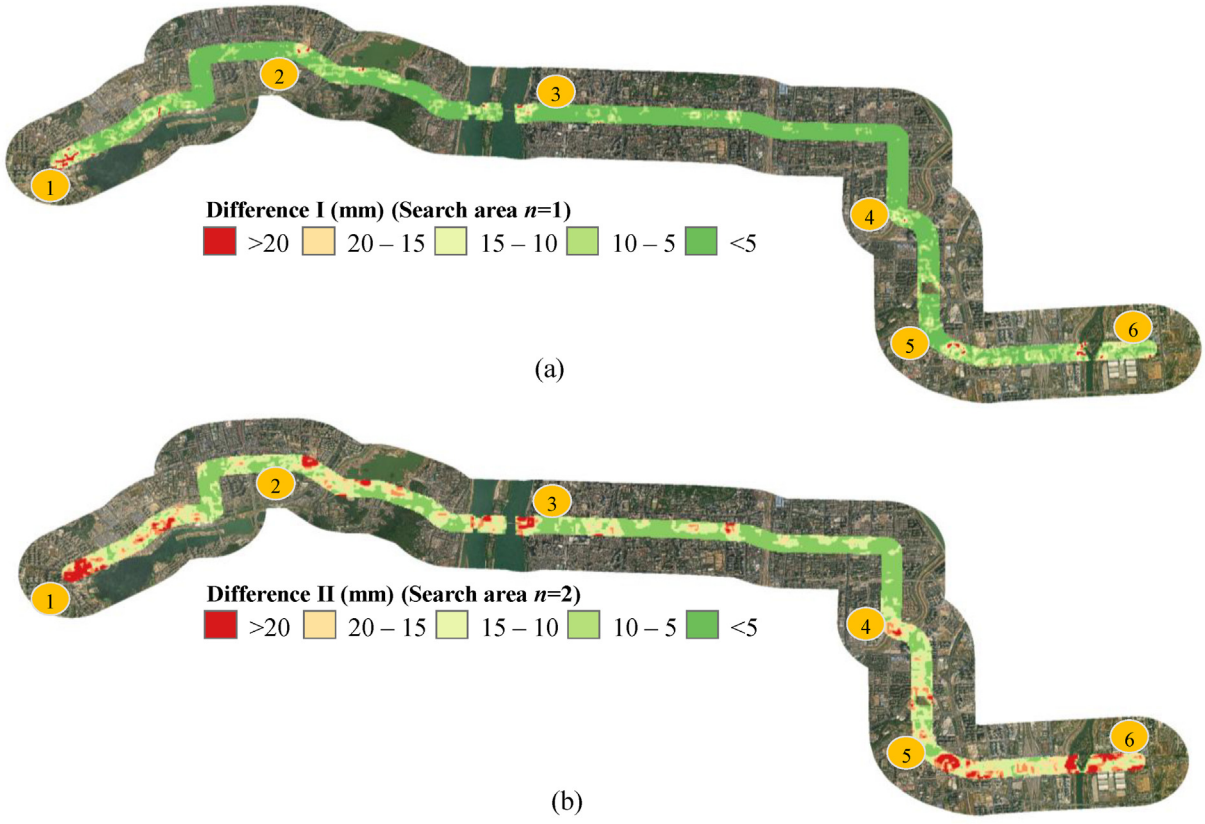

Fig. 16. (a) Settlement difference at search unit $n = 1$, and (b) settlement difference at search unit $n = 2$.

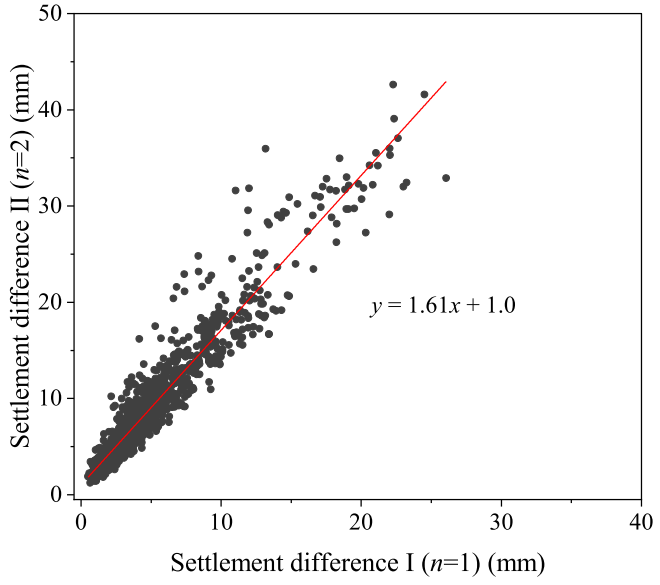

Fig. 17. Correlation chart of settlement differences between the two search units.

disturbance source is located south of the metro line but farther away, resulting in a relatively smaller impact. Figure 19(d) corresponds to the L2-4 region, where the disturbance source is located southwest of the metro line. The satellite imagery clearly records the transition from green space to high-rise buildings, with serious cracks and spalling in the area. Figure 19(e) shows the L2-5 region, where the disturbance source is directly above the metro line, and severe leakage occurred in the metro at this location. Figure 19(f) shows the L2-6 region, which crosses the Liuyang River and belongs to a water-rich layer. This area also experienced artificial construction disturbances above the metro. Survey data indicate severe leakage issues in this tunnel section.

Figure 20 presents the settlement difference search results for different metro lines. Figure 20(a) shows the settlement difference results for Metro Line 1, where two sections with significant settlement differences, L1-1 and L1-2, are identified. Figure 20(b) displays the settlement difference results for Metro Line 3, where three sections with significant settlement differences, L3-1, L3-2, and L3-3, are observed. Figure 20(c) shows the settlement difference results for Metro Line 4, with three sections, L4-1, L4-2, and L4-3, exhibiting significant settlement differences. Figure 20(d) presents the settlement difference results for Metro Line 5, where three sections, L5-1, L5-2, and L5-3, show notable settlement differences. Figure 20(e) illustrates the settlement difference results for Metro Line 6, with three sections, L6-1 and L6-2, showing significant settlement differences.

Figure 21 presents the satellite image comparison of areas with significant settlement differences, corresponding

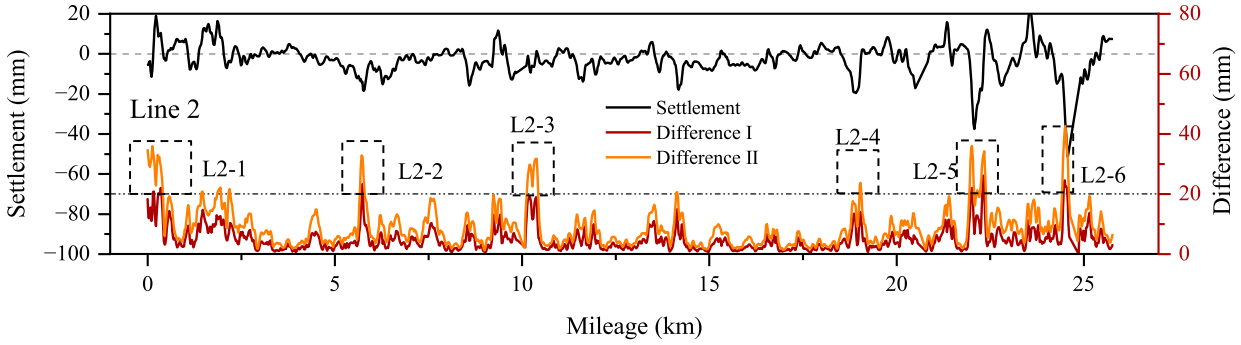

Fig. 18. Settlement results and settlement difference results of Metro Line 2.

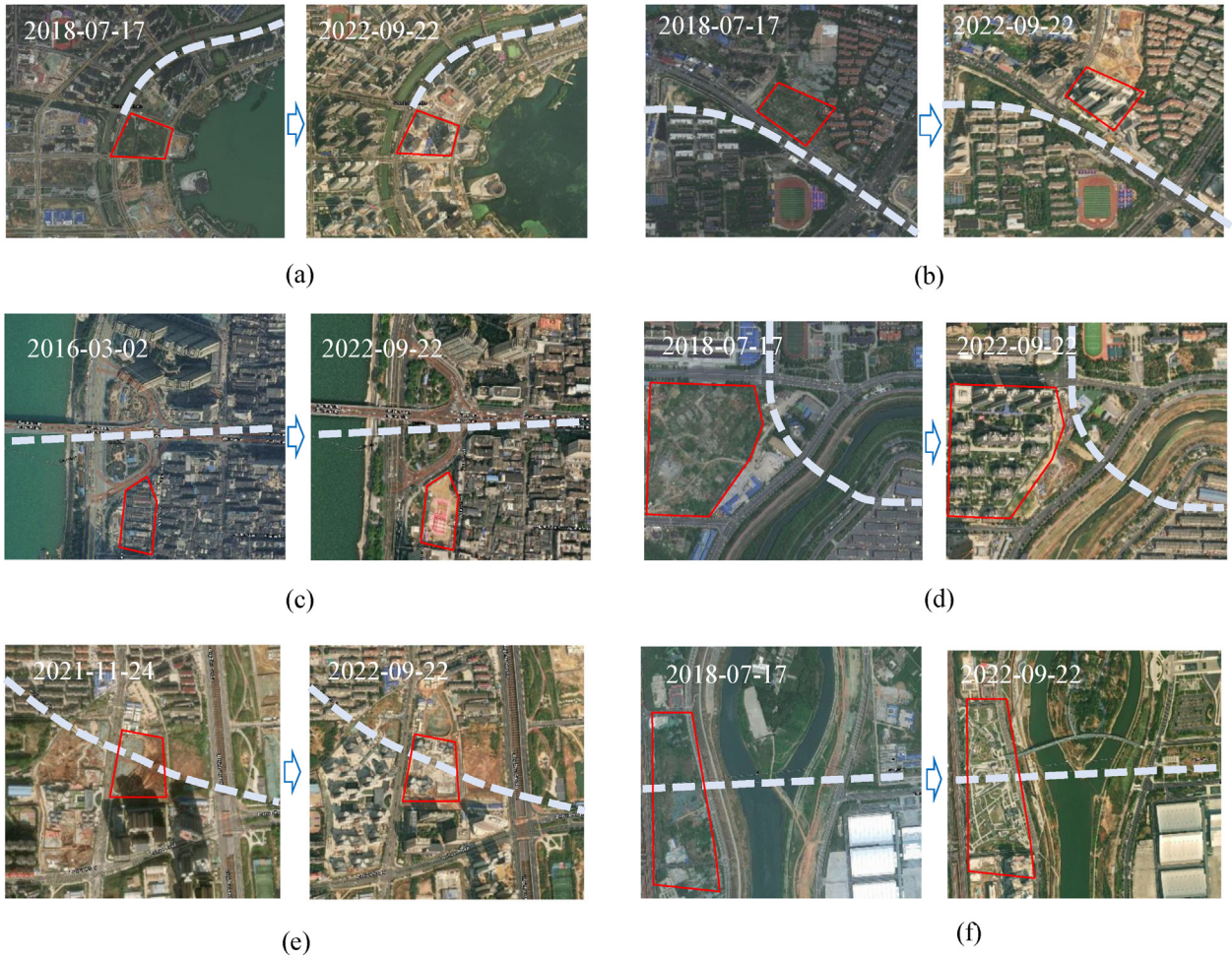

Fig. 19. Satellite image comparison before and after for the six areas with significant settlement differences along Metro Line 2. (a) L2-1, (b) L2-2, (c) L2-3, (d) L2-4, (e) L2-5, and (f) L2-6 (and L4-3).

to the regions marked in Fig. 20. The images show that almost all sections of the surface exhibit some topographical changes, with particularly noticeable traces of human construction. This demonstrates the effectiveness of the settlement difference metric. Additionally, the disturbance areas can be divided into two categories: one involving disturbances beside the metro lines (Fig. 21(a), (b), (e), and (h)–(k)), and the other involving construction directly above the metro lines (Fig. 21(c), (f), (l)). In terms of the size of the disturbance sources, there are disturbances from single building construction projects (Fig. 21(e)), as well as larger-scale disturbances from the construction of multiple buildings or even entire residential complexes (Fig. 21(f) and (k)). Notably, Fig. 21(d) shows a location with no

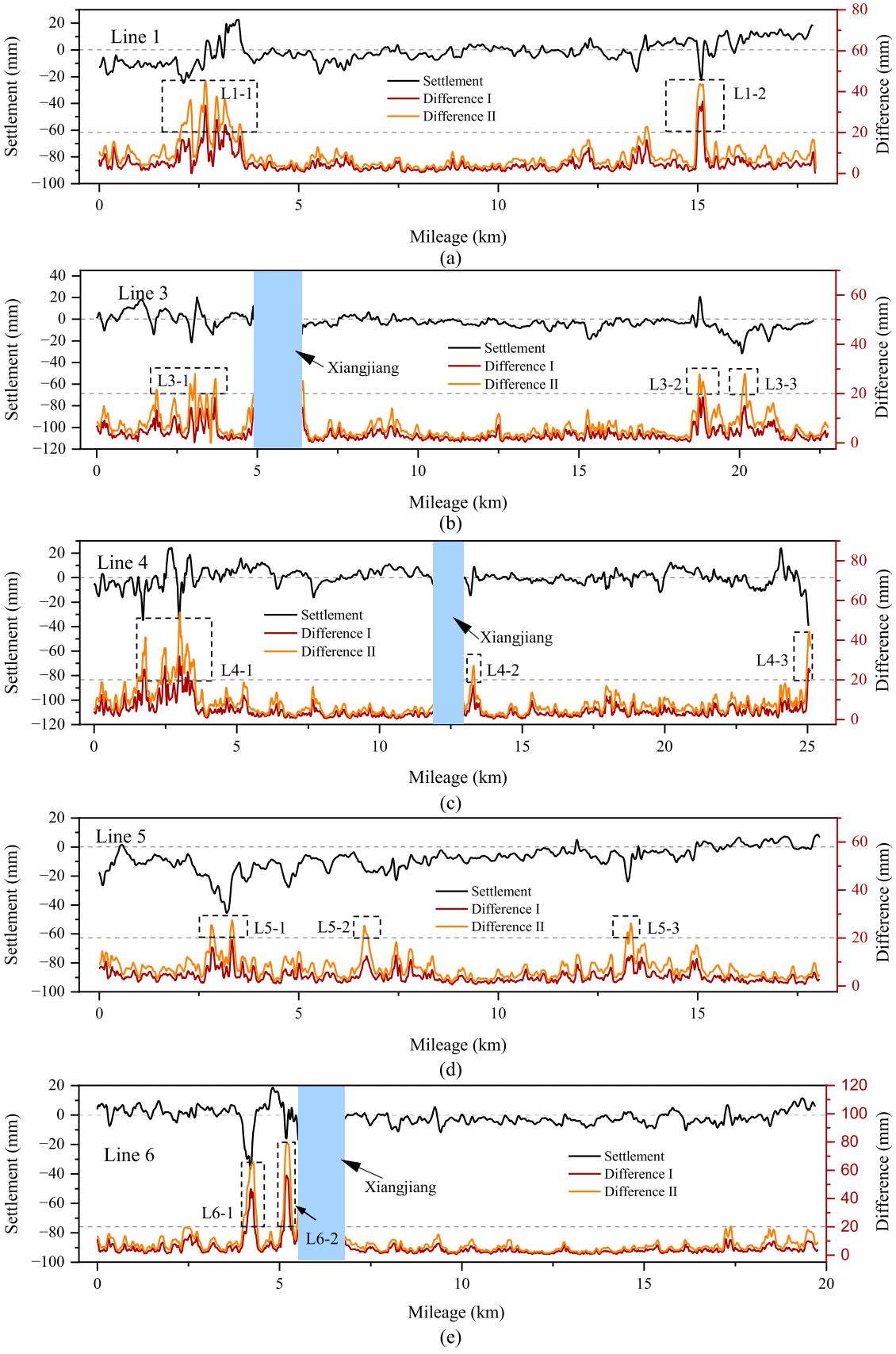

Fig. 20. Settlement curves and differential settlement curves along metro lines.

Fig. 21. Satellite image comparison of areas with significant settlement differences. (a) L1-1, (b) L1-2, (c) L3-1, (d) L3-2, (e) L3-3, (f) L4-1, (g) L4-2, (h) L5-1, (i) L5-2, (j) L5-3, (k) L6-1, and (l) L6-2.

apparent surface construction. However, its proximity to a river suggests that the observed settlement may be attributed to natural causes, such as soil consolidation.

Figure 22 presents the statistical characteristics of data for areas with significant settlement. Figure 22(a) shows the relationship between cumulative settlement and settle-

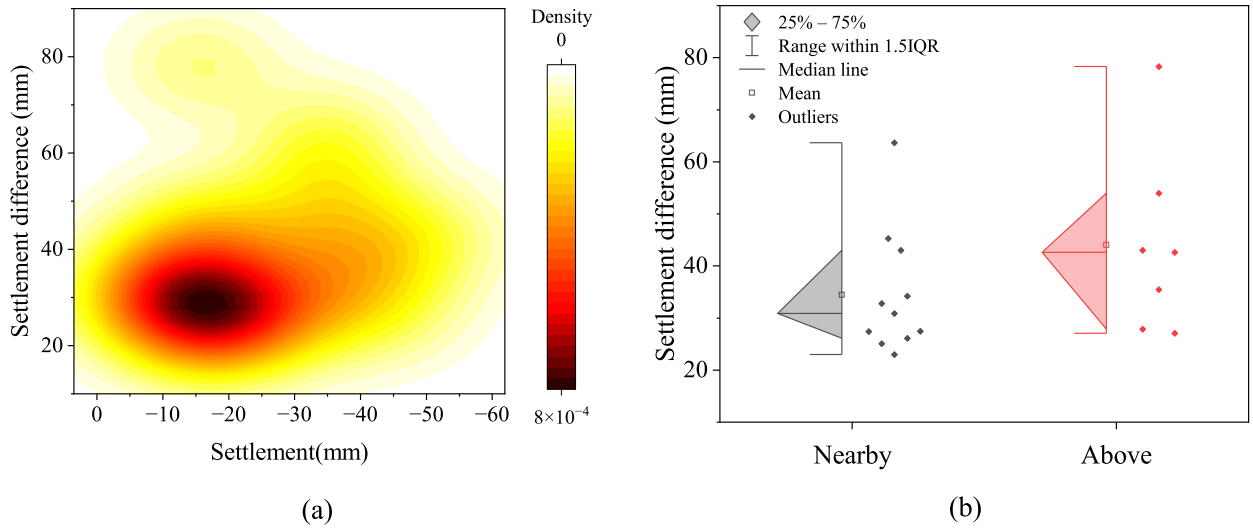

Fig. 22. Data characteristics of areas with significant settlement differences.

ment difference, with cumulative settlement on the *x*-axis and settlement difference on the *y*-axis. The plot indicates that the settlement difference is mainly concentrated around 30 mm, while the cumulative settlement is concentrated around −20 mm. Figure 22(b) divides the settlement difference data into two groups based on the position of the disturbance source. It can be seen that when the disturbance source is located directly above the metro line, the average settlement difference is 42 mm; when the disturbance source is nearby, the average settlement difference is 34 mm. Overall, the settlement difference is close to 30 mm, and almost all areas exhibit disturbance sources. This also supports the rationale for selecting the settlement difference as the metric in this study.

5.3 Limitations and challenges

This study presents a preliminary risk assessment of metro-adjacent areas using the SBAS-InSAR technique, aiming to explore the underlying causes of potential risks. The proposed technical framework shows promise for large-scale, long-term monitoring of urban infrastructure such as metro systems and could serve as a reference for similar future studies.

However, several limitations and challenges were encountered during the implementation process. First, regarding data sources, the spatial resolution of Sentinel-1 SAR imagery makes it difficult to accurately distinguish between ground-level subsidence and deformation occurring on building rooftops in densely built urban areas. Future studies may benefit from employing higher-resolution satellite data, such as that from Ludtan-1 or TerraSAR-X, to improve the spatial accuracy of the deformation analysis. Second, this study identifies ground construction activity as the main disturbance factor in metro-adjacent areas by combining indicators such as settlement rate, differential settlement, and historical satellite imagery. However, it remains challenging to fully isolate the impact of other contributing factors, such as soil consolidation, post-construction tunnel settlement, or their combined effects. While the specific cause of deformation may be difficult to determine precisely, it is important to note that any form of ground disturbance within the metro vicinity can potentially increase the structural risk to underground infrastructure. Lastly, we hope future work can incorporate higher-precision satellite datasets and develop methodologies to differentiate among various risk factors. This will allow for a more comprehensive understanding of how different mechanisms contribute to subsidence-related risks and further expand the application of InSAR technologies in infrastructure risk assessment, particularly in complex urban metro systems.

6 Conclusions

This study analyzed surface settlement in Changsha from January 2017 to July 2023 using a dataset of 147 Sentinel satellite images processed with the SBAS technique. By examining the settlement rate characteristics of three typical regions, the study validated the capability of InSAR technology to identify urban construction areas. A grid search algorithm was then employed to identify settlement differences within the metro vicinity. Finally, a risk assessment of the Changsha metro operation was conducted based on settlement rates, settlement differences, and subsurface environmental factors in the metro vicinity. The main conclusions are as follows:

(1) The SBAS-InSAR technique effectively identifies urban construction processes and offers the advantages of large-scale, long-term monitoring. It can accurately record surface settlement during the given study period. Combined with historical satellite imagery, it was found that in areas with significant con-

struction activities, the average annual settlement rate typically exceeds −6 mm/yr, with some regions reaching up to −10 mm/yr. In contrast, most areas without ground disturbance usually experience surface settlement not exceeding −2 mm/yr.

(2) Satellite imagery analysis of metro areas with settlement differences greater than 20 mm revealed that most of these regions are influenced by clear disturbance sources, such as adjacent or above foundation pit excavation. A few regions show no visible signs of construction, and the settlement differences in these areas may result from non-construction factors such as soil consolidation.

(3) A risk assessment of Changsha's metro system, based on multi-source data, showed that the overall risk level of the metro system is relatively low, with some areas being categorized as "high risk." In the "high risk" sections, Metro Line 2 and Metro Line 6 account for 32.7% and 20%, respectively. Some tunnel sections of Line 2 are exhibiting cracks, leakage, and concrete spalling.

This study provides valuable insights into identifying potential hazard points in metro areas, monitoring settlement during both construction and operation phases, and offers scientific support for metro engineering project risk assessment and management strategies.

Data availability

The data that support the findings of this study are available from the corresponding author upon reasonable request.

CRediT authorship contribution statement

Zhiwen Xu: Writing – original draft, Validation, Software, Project administration, Funding acquisition. **Suhua Zhou:** Writing – original draft, Resources, Project administration, Methodology, Funding acquisition, Conceptualization. **Qingshan Zhang:** Software, Investigation, Formal analysis, Data curation. **Jiuchang Zhang:** Resources, Methodology, Conceptualization. **Chuting Huang:** Visualization, Software, Resources, Data curation.

Declaration of competing interest

The authors declare that they have no known competing financial interests or personal relationships that could have appeared to influence the work reported in this paper.

Acknowledgement

The work presented in this paper was financially supported by the Postgraduate Scientific Research Innovation Project of Hunan Province (CX20240432), the Key Laboratory of Geological Safety of Coastal Urban Underground Space, Ministry of Natural Resources (BHKF2023Y04), the Natural Science Foundation of Changsha (Grant Nos. kq2208031 and kq2402072), and the Natural Resources Science and Technology Project of Fujian Province (KY-070000-04-2021-025).

References

Ao, Z., Hu, X., Tao, S., Hu, X., Wang, G., Li, M., Wang, F., Hu, L., Liang, X., Xiao, J., & Yusup, A. (2024). A national-scale assessment of land subsidence in China's major cities. *Science, 384*(6693), 301–306.

Berardino, P., Fornaro, G., Lanari, R., & Sansosti, E. (2002). A new algorithm for surface deformation monitoring based on small baseline differential SAR interferograms. *IEEE Transactions on Geoscience & Remote Sensing, 40*(11), 2375–2383.

Chakeri, H., & Ünver, B. (2014). A new equation for estimating the maximum surface settlement above tunnels excavated in soft ground. *Environmental Earth Sciences, 71*(7), 3195–3210.

Chang, C. T., Sun, C. W., Duann, S. W., & Hwang, R. N. (2001). Response of a Taipei Rapid Transit System (TRTS) tunnel to adjacent excavation. *Tunnelling and Underground Space Technology, 16*(3), 151–158.

Chaussard, E., Amelung, F., Abidin, H., & Hong, S. H. (2013). Sinking cities in Indonesia: ALOS PALSAR detects rapid subsidence due to groundwater and gas extraction. *Remote Sensing of Environment, 128*, 150–161.

Chen, R., Meng, F., Li, Z., Ye, Y., & Ye, J. (2016). Investigation of response of metro tunnels due to adjacent large excavation and protective measures in soft soils. *Tunnelling and Underground Space Technology, 58*, 224–235.

Cigna, F., & Tapete, D. (2021). Sentinel-1 big data processing with P-SBAS InSAR in the geohazards exploitation platform: An experiment on coastal land subsidence and landslides in Italy. *Remote Sensing, 13*(5), 1–26.

Di, H., Zhou, S., Yao, X., & Tian, Z. (2021). In situ grouting tests for differential settlement treatment of a cut-and-cover metro tunnel in soft soils. *Bulletin of Engineering Geology and the Environment, 80*(8), 6415–6427.

Doyle, M. R. (2016). From hydro/geology to the streetscape: Evaluating urban underground resource potential. *Tunnelling and Underground Space Technology, 55*, 83–95.

Esmatkhah Irani, A., Azadi, A., Nikbakht, M., Azarafza, M., Hajialilue Bonab, M., & Behrooz Sarand, F. (2022). GIS-based settlement risk assessment and its effect on surface structures: A case study for the Tabriz Metro—line 1. *Geotechnical and Geological Engineering, 40*(10), 5081–5102.

Ferretti, A., Prati, C., & Rocca, F. (2001). Permanent scatterers in SAR interferometry. *IEEE Transactions on Geoscience and Remote Sensing, 39*(1), 8–20.

Giardina, G., Milillo, P., DeJong, M. J., Perissin, D., & Milillo, G. (2019). Evaluation of InSAR monitoring data for post-tunnelling settlement damage assessment. *Structural Control and Health Monitoring, 26*(2).

He, Y., Li, X., Yang, J., Liu, Y., Yang, G., Hu, M., Chen, S., Yao, H., Wang, L., & Xiong, X. (2024). Urban land subsidence monitoring and risk assessment using the point target based SBAS-InSAR method: A case study of Changsha City. *Remote Sensing Letters, 15*(7), 689–699.

Hrysiewicz, A., Williamson, J., Evans, C. D., Jovani-Sancho, A. J., Callaghan, N., Lyons, J., White, J., Kowalska, J., Menichino, N., & Holohan, E. P. (2024). Estimation and validation of InSAR-derived surface displacements at temperate raised peatlands. *Remote Sensing of Environment, 311*, 114232.

Hu, R. L., Yue, Z. Q., Wang, L. C., & Wang, S. J. (2004). Review on current status and challenging issues of land subsidence in China. *Engineering Geology, 76*(1–2), 65–77.

Huang, Z., Fu, H., Chen, W., Zhang, J., & Huang, H. (2018). Damage detection and quantitative analysis of shield tunnel structure. *Automation in Construction, 94*(May), 303–316.

Liu, B., Zhang, D. W., Yang, C., & Zhang, Q. B. (2020). Long-term performance of metro tunnels induced by adjacent large deep excavation and protective measures in Nanjing silty clay. *Tunnelling and Underground Space Technology, 95*, 103147.

Liu, J. C., & Tan, Y. (2023). Review of through-wall leaking incidents during excavation of the subway stations of Nantong metro line 1 in

thick water-rich sandy strata. *Tunnelling and Underground Space Technology, 135*, 105056.
Liu, Y., Cao, W., Shi, Z., Yue, Q., Chen, T., Tian, L., Zhong, R., & Liu, Y. (2023). Evaluation of post-tunneling aging buildings using the InSAR nonuniform settlement index. *Remote Sensing, 15*(14), 3467.
Lu, Y., Jin, C., Wang, Q., Han, T., Li, G., Zhong, X., & Chen, G. (2023). Combining InSAR and infrared thermography with numerical simulation to identify the unstable slope of open-pit: Qidashan case study, China. *Landslides, 20*(9), 1961–1974.
Ma, F., Zhao, H., Zhang, Y., Guo, J., Wei, A., Wu, Z., & Zhang, Y. (2012). GPS monitoring and analysis of ground movement and deformation induced by transition from open-pit to underground mining. *Journal of Rock Mechanics and Geotechnical Engineering, 4*(1), 82–87.
Ma, P., Lin, H., Wang, W., Yu, H., Chen, F., Jiang, L., Zhou, L., Zhang, Z., Shi, G., & Wang, J. (2022). Toward Fine Surveillance: A review of multitemporal interferometric synthetic aperture radar for infrastructure health monitoring. *IEEE Geoscience and Remote Sensing Magazine, 10*(1), 207–230.
Meng, F. Y., Chen, R. P., Wu, H. N., Xie, S. W., & Liu, Y. (2020). Observed behaviors of a long and deep excavation and collinear underlying tunnels in Shenzhen granite residual soil. *Tunnelling and Underground Space Technology, 103*, 103504.
Mehrabi, A., Derakhshani, R., Nilfouroushan, F., Rahnamarad, J., & Azarafza, M. (2023). Spatiotemporal subsidence over Pabdana coal mine Kerman Province, central Iran using time-series of Sentinel-1 remote sensing imagery. *Episodes, 46*(1), 19–33.
Ministry of Housing and Urban-Rural Development of the People's Republic of China (2013). *GB 50911—2013: Code for monitoring measurement of urban rail transit engineering* (in Chinese).
Perissin, D., Wang, Z., & Lin, H. (2012). Shanghai subway tunnels and highways monitoring through Cosmo-SkyMed Persistent Scatterers. *ISPRS Journal of Photogrammetry and Remote Sensing, 73*(9), 58–67.
Psimoulis, P., Ghilardi, M., Fouache, E., & Stiros, S. (2007). Subsidence and evolution of the Thessaloniki plain, Greece, based on historical leveling and GPS data. *Engineering Geology, 90*(1–2), 55–70.
Qin, X., Zhang, L., Yang, M., Luo, H., Liao, M., & Ding, X. (2018). Mapping surface deformation and thermal dilation of arch bridges by structure-driven multi-temporal DInSAR analysis. *Remote Sensing of Environment, 216*(129), 71–90.
Saaty, T. L. (1994). To make a decision: The analytic. *Interfaces, 24*(6), 19–43.
Shen, S. L., Wu, H. N., Cui, Y. J., & Yin, Z. Y. (2014). Long-term settlement behaviour of metro tunnels in the soft deposits of Shanghai. *Tunnelling and Underground Space Technology, 40*, 309–323.
Strozzi, T., Caduff, R., Wegmüller, U., Raetzo, H., & Hauser, M. (2017). Widespread surface subsidence measured with satellite SAR interferometry in the Swiss alpine range associated with the construction of the Gotthard Base Tunnel. *Remote Sensing of Environment, 190*, 1–12.
Tan, Y., Zhu, H., Peng, F., Karlsrud, K., & Wei, B. (2017). Characterization of semi-top-down excavation for subway station in Shanghai soft ground. *Tunnelling and Underground Space Technology, 68*, 244–261.
Tongji University, & Guangzhou Metro Design & Research Institute Co., Ltd. (2018). *CJJ/T 289—2018: Technical standard for maintenance of tunnel structures in urban rail transit* (in Chinese).
Wan, M. S. P., Standing, J. R., Potts, D. M., & Burland, J. B. (2017). Measured short-term ground surface response to EPBM tunnelling in London Clay. *Géotechnique, 67*(5), 420–445.
Wu, H. N., Xu, X. P., Chen, R. P., Liu, Y., Cheng, H. Z., & Xiao, C. (2024). Observed uplift behaviors of segmental lining during shield tunneling in hard rock: A case study from Changsha, China. *Tunnelling and Underground Space Technology, 150*, 105816.
Xu, Y. C., Li, J., Wu, L. X., Guo, L., & Xu, H. D. (2021). Monitoring ground subsidence in Changsha urban area between 2017-2020 based on SBAS-InSAR. *Hydrographic Surveying and Charting, 41*(5), 37–42 (in Chinese).
Xu, Z., Zhou, S., Zhang, C., Yang, M., & Jiang, M. (2023). A Bayesian network model for suitability evaluation of underground space development in urban areas: The case of Changsha, China. *Journal of Cleaner Production, 418*, 138135.
Yan, F., Shangguan, W., Zhang, J., & Hu, B. (2020). Depth-to-bedrock map of China at a spatial resolution of 100 meters. *Scientific Data, 7*(1), 1–13.
Yang, M., Wang, R., Li, M., & Liao, M. (2022). A PSI targets characterization approach to interpreting surface displacement signals: A case study of the Shanghai metro tunnels. *Remote Sensing of Environment, 280*, 113115.
Yang, Q., Ke, Y., Zhang, D., Chen, B., Gong, H., Lv, M., Zhu, L., & Li, X. (2018). Multi-scale analysis of the relationship between land subsidence and buildings: A case study in an eastern Beijing Urban Area using the PS-InSAR technique. *Remote Sensing, 10*(7), 1006.
Zeng, P., Feng, B., Dai, K., Li, T., Fan, X., & Sun, X. (2024). Can satellite InSAR innovate the way of large landslide early warning?. *Engineering Geology, 342*, 107771.
Zhang, Y., Jiao, Y. Y., He, L. L., Tan, F., Zhu, H. M., Wei, H. L., & Zhang, Q. B. (2024). Susceptibility mapping and risk assessment of urban sinkholes based on grey system theory. *Tunnelling and Underground Space Technology, 152*, 105893.
Zheng, G., Du, Y. M., Diao, Y., Deng, X., Zhu, G. P., & Zhang, L. M. (2016). Influenced zones for deformation of existing tunnels adjacent to excavations. *Chinese Journal of Geotechnical Engineering, 38*(4), 599–612 (in Chinese).
Zheng, G., Liu, Q. C., & Deng, X. (2013). Numerical analysis of effect of excavation on underlying existing metro tunnel and deformation control. *Rock and Soil Mechanics, 34*(4), 1459–1468.
Zhou, D., Li, X., Wang, Q., Wang, R., Wang, T., Gu, Q., & Xin, Y. (2019). GIS-based urban underground space resources evaluation toward three-dimensional land planning: A case study in Nantong, China. *Tunnelling and Underground Space Technology, 84*, 1–10.